Mineralium Deposita
https://doi.org/10.1007/s00126-020-00997-3

ARTICLE

Late Cretaceous granitic magmatism and Sn mineralization in the giant Yinyan porphyry tin deposit, South China: constraints from zircon and cassiterite U–Pb and molybdenite Re–Os geochronology

Peng-Cheng Hu[1,2] · Wei-Guang Zhu[1] · Hong Zhong[1,2] · Rong-Qing Zhang[3] · Xiao-Yu Zhao[1,2] · Wei Mao[1]

Received: 25 December 2019 / Accepted: 9 June 2020

Abstract

The Yinyan porphyry tin deposit in western Guangdong is spatially associated with quartz porphyry and granite porphyry. LA–ICP–MS zircon U–Pb dating defined an emplacement age of 78.5 ± 0.4 Ma for the quartz porphyry and 79.2 ± 0.9 Ma for the granite porphyry. LA–ICP–MS cassiterite U–Pb dating yielded Tera–Wasserburg lower intercept ages of 78.5 ± 0.6, 78.6 ± 1.2, and 78.2 ± 0.7 Ma, for cassiterite from a cassiterite–sulfide vein, cassiterite–sulfide ore, and a cassiterite–topaz–quartz stringer, respectively. Re–Os dating of molybdenite from seven different veins yielded an isochron age of 77.0 ± 0.5 Ma. All these new age data are indistinguishable within analytical uncertainty and, therefore, indicate a genetic relationship between the Sn mineralization and the porphyry magmatism in the Yinyan deposit. The REE tetrad effect and very low Nb/Ta and Zr/Hf ratios indicate that the quartz porphyry and the granite porphyry are highly evolved. The U–Pb dated cassiterite is enriched in Fe, W, and U and in high field strength elements (HFSEs) such as Zr, Hf, Nb, and Ta. The high Fe, Nb, and Ta contents may be responsible for the dark luminescence of cassiterite in CL images. The Zr/Hf ratio of cassiterite may potentially be used to distinguish the mineralization type. Cassiterite from pegmatites has lower Zr/Hf ratios (~ 5–6) in comparison with granite/greisen-related (~ 9–30) cassiterite. Cassiterite from the early hydrothermal stage typically contains higher amounts of Ti, Nb, Ta, Zr, and Hf than that from the late hydrothermal stage. In combination with published geochronological data of other Sn–W deposits in the western Guangdong Province, two Sn–W metallogenic events at ca. 85 and 77–80 Ma have been identified. These two metallogenic events are part of a larger-scale 75–100 Ma Sn–W mineralization event in South China, which we suggest was probably related to the subduction of the Neo-Tethyan oceanic plate.

Keywords LA–ICP–MS zircon and cassiterite U–Pb dating · Molybdenite Re–Os dating · Late Cretaceous Sn–W mineralization · Yinyan tin deposit

Editorial handling: B. Lehmann

Electronic supplementary material The online version of this article (https://doi.org/10.1007/s00126-020-00997-3) contains supplementary material, which is available to authorized users.

✉ Wei-Guang Zhu
zhuweiguang@vip.gyig.ac.cn

[1] State Key Laboratory of Ore Deposit Geochemistry, Institute of Geochemistry, Chinese Academy of Sciences, Guiyang 550081, China

[2] University of Chinese Academy of Sciences, Beijing 100049, China

[3] State Key Laboratory for Mineral Deposits Research, School of Earth Sciences and Engineering, Nanjing University, Xianlin University Town, Nanjing 210023, China

Introduction

South China is renowned for its Mesozoic granite magmatism and associated large-scale W–Sn mineralization (Hua and Mao 1999; Zhou et al. 2006; Sun et al. 2012). The temporal and spatial distribution patterns between the W and Sn mineralization in South China are different (Fig. 1b). The W (±Sn) deposits mainly cluster in the Nanling Range and the newly defined Jiangnan Tungsten Belt (Mao et al. 2017), and the corresponding mineralization ages are mainly in the period 150–160 Ma (Mao et al. 2008, 2013) and 121–153 Ma (Mao et al. 2017; Kong et al. 2018). In contrast, the Sn (±W) deposits are distributed mainly in the Southeast Coast and southwestern–southern parts of South China, and they

Published online: 22 July 2020

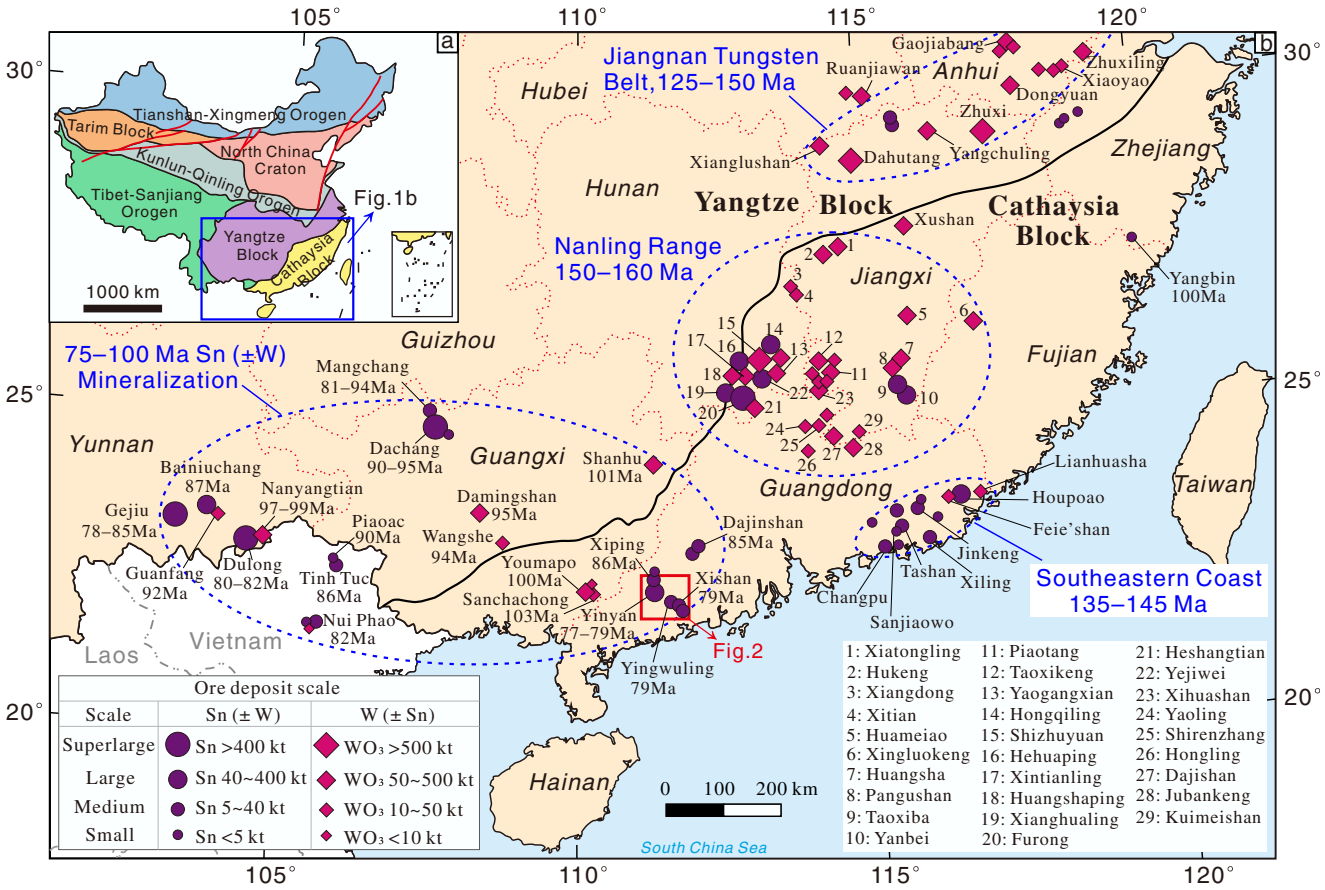

Fig. 1 **a** Simplified tectonic map of China (after Pan et al. 2009). **b** Distribution of major Mesozoic W–Sn deposits in South China and northern Vietnam (compiled from Mao et al. 2008, 2013, 2017; Cheng et al. 2016; Wang et al. 2019, with base map adapted from Zhao and Wu 2007)

formed mainly in the period 135–145 Ma (Yan et al. 2017; Liu et al. 2018) and 80–100 Ma (Cheng et al. 2016; Zheng et al. 2017a, b), respectively. It is worth noting that the 80–100 Ma Sn deposits located in southeastern Yunnan, Guangxi, and western Guangdong, including the world-class Gejiu, Dulong, and Dachang tin-polymetallic deposits, contribute most of the tin resources of China (Chen et al. 2015). In the western part of Guangdong, there are many Sn–W deposits that have formation ages of about 80 Ma, similar to the world-class Gejiu and Dulong deposits (Fig. 1b). These deposits are represented by the Yinyan Sn deposit and Yinwuling and Xishan W–Sn deposits, but little attention had been paid to them until recently (Zheng et al. 2016, 2017a, b; Zhang et al. 2017b, 2018). However, as these deposits are located in the junction zone of the Pacific and Tethyan tectonic domains (Zhou et al. 2008), it has been a hot topic of debate which tectonic setting was responsible for their formation (Cheng et al. 2016; Sun 2016; Zhang et al. 2017b, 2018; Zheng et al. 2017a, b).

The Yinyan Sn deposit, located in the western part of Guangdong (Fig. 1b) and discovered by Geological Team 704 in 1979 (Zhu et al. 1989), is the first recognized typical porphyry tin deposit in China (Guan et al. 1985, 1988; Huang and Zhang 1989). With total Sn metal reserves of 0.14 Mt (average grade of 0.36% Sn) accompanied by W and Mo as by-products, the Yinyan deposit is the largest among the three typical porphyry tin deposits in China, i.e., Yinyan in Guangdong, Yanbei in Jiangxi, and Yejiwei in Hunan (Zheng et al. 2016). Previous studies on the deposit were carried out mainly in the 1980s and were focused on the geological characteristics of the deposit (Wu 1983; Li 1988), the petrology and geochemistry of the host granites (Hu 1989; Zhu et al. 1989), and fluid inclusions (Xie et al. 1988). The geochronology of the mineralization-related porphyries has also been studied but only the whole-rock/single mineral K–Ar or Rb–Sr methods were used for dating and they yielded scattered data ranging from 75.6 to 92 Ma (Guan et al. 1985, 1988; Hu 1989; Shen et al. 1996). Recently, Zheng et al. (2016) obtained a molybdenite Re–Os isochron age of 78.8 ± 2.6 Ma. Since these ages are not consistent with each other, the timing of and the genetic relationships between the mineralization and the magmatism in the Yinyan tin deposit remain equivocal.

In this paper, we utilize cassiterite and zircon LA–ICP–MS U–Pb dating together with molybdenite Re–Os dating to constrain the timing of Sn mineralization and granite magmatism

in the Yinyan tin deposit. In addition, trace element geochemistry of porphyries and cassiterite is used to constrain the degree of magma differentiation and to reveal the mineralization features. Finally, we put forward a geodynamic model for the Late Cretaceous Sn–W metallogenic event in western Guangdong and South China in general.

Regional geological setting

The South China Block consists of the Yangtze Block to the northwest and the Cathaysia Block to the southeast (Charvet et al. 1996). Our study area is located in the southwestern part of the Cathaysia Block (Fig. 1b) and has undergone multiple tectonic overprint which resulted in the formation of complex structural patterns dominated by a NE to NNE trend (Peng et al. 1995a; Zheng et al. 2015). The major fault is the NE–SW to NNE–SSW trending Wuchuan–Sihui deep-seated fault (also termed the Wuchuan–Sihui Shear Zone, Fig. 2), which may extend over the depth of the lithosphere and underwent strike-slip shearing at around 133 Ma (Shao et al. 1995). The Wuchuan–Sihui deep-seated fault divides the study area into the Yunkai Massif to the west and the Yangchun Basin to the southeast (Peng et al. 1995b; Yu et al. 1998).

The Yunkai Massif is a Caledonian metamorphic massif (Wang et al. 2007). The basement of Yunkai Massif is mainly composed of the late Neoproterozoic–early Paleozoic (Zhou et al. 2015; Han et al. 2017) Gaozhou Complex and Yunkai Group, which are overlain by weakly metamorphosed to unmetamorphosed Cambrian–Devonian strata (Wang et al. 1998). The Gaozhou Complex consists mainly of amphibolite (locally granulite) facies, supracrustal rocks, and migmatites, whereas the Yunkai Group comprises primarily meta-sedimentary/volcanic rocks of greenschist facies (Zhong et al.

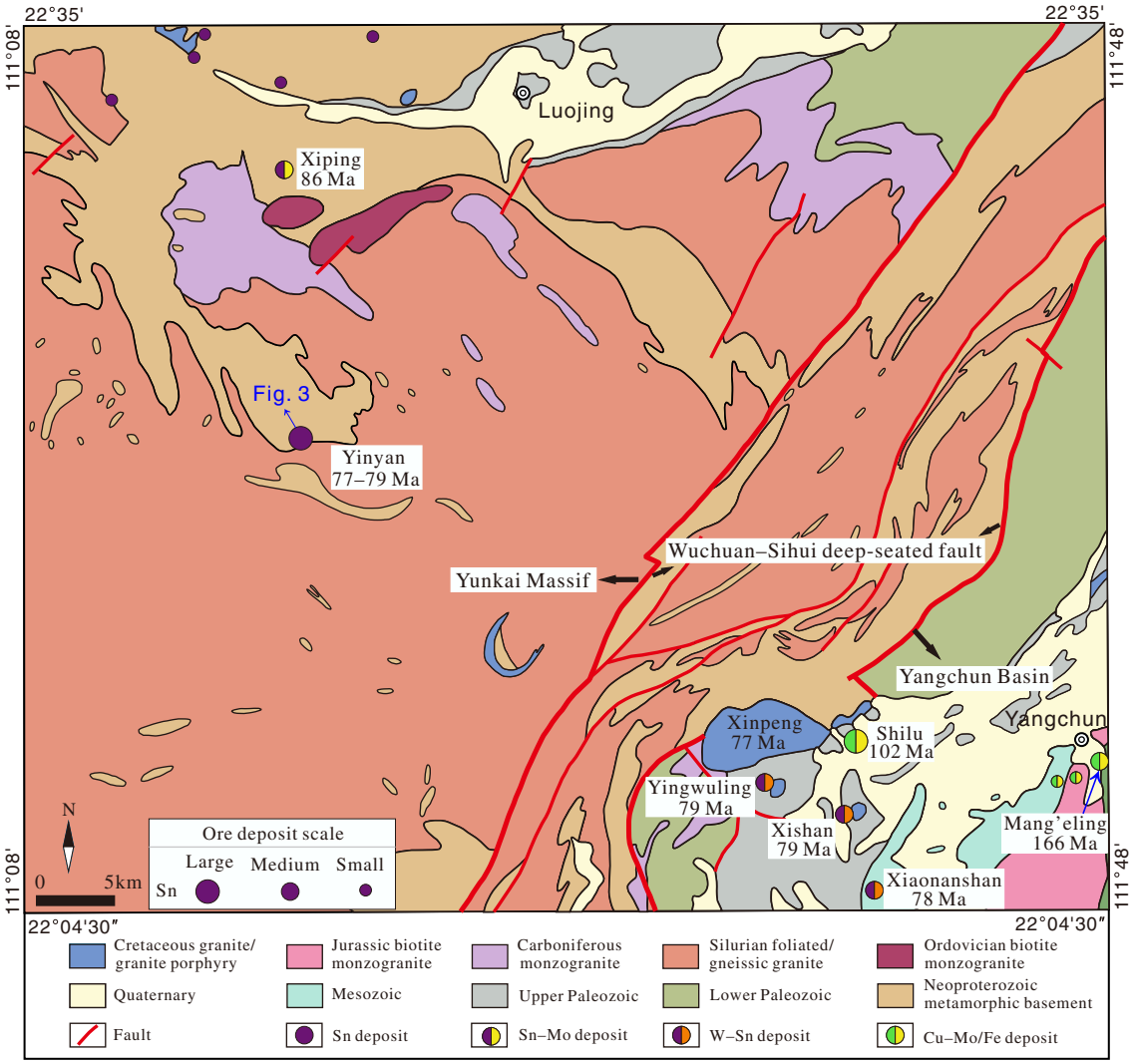

Fig. 2 Simplified geological map of the Yunkai Massif and Yangchun Basin, western Guangdong Province (modified after the 1:250,000 Yangchun geological map). The data sources of Sn–W deposits age are shown in Supplemental Table D. The classification standard of the ore deposits scale is identical to those in Fig. 1b

1996; Wang et al. 1998; Wan et al. 2010). Intrusive rocks are widely distributed in the Yunkai Massif (Fig. 2). The most widespread Silurian foliated/gneissic granites were formed mainly at 415–450 Ma (Wang et al. 2007; Wan et al. 2010) and underwent deformation and metamorphism during the period 200–250 Ma (Chen et al. 2017; Ke et al. 2018). Cretaceous granites are sporadically exposed, but all Sn–W deposits in the Yunkai Massif are associated with them, for instance, the Yinyan tin deposit and the Xiping Sn–Mo polymetallic deposit.

The Yangchun Basin is an Indosinian graben basin (Yu et al. 1998). The basement rocks in the Yangchun Basin consist mainly of Cambrian low-grade metamorphic flysch and sandy shales. The cover rocks comprise the Upper Paleozoic, which mainly includes carbonate rocks, neritic clastic rocks, and sandy shales. The uppermost strata are Mesozoic terrestrial clastic rocks that sporadically are exposed (Yu et al. 1998). Unlike the Yunkai Massif, igneous rocks in the Yangchun Basin are dominated by the Mesozoic granitic rocks (Zheng et al. 2015), whereas Paleozoic granitic rocks are rare. It should be noted that all W–Sn and Cu–Mo (±Fe) mineralization in the basin is related to the Jurassic and Cretaceous intermediate–felsic intrusions, and different types of intrusions are associated with different mineralization types (Zheng et al. 2015). For example, the Shilu Cu–Mo deposit is related to ~ 104 Ma granodiorite (Zhang et al. 2017a), and the Xishan and Yingwuling Sn–W deposits are related to ~ 79 Ma granites (Zhang et al. 2017b, 2018; Zheng et al. 2017a, b).

Geology of the Yinyan porphyry tin deposit

The Yinyan tin deposit (22° 21′ 04″ N, 111°18′ 03″ E) is located 30 km west of the Wuchuan–Sihui deep-seated fault (Li 1988). The exposed strata in the mine area are the Neoproterozoic Lankeng Formation, which is a subunit of the aforementioned Yunkai Group (Zhou et al. 1996) and consists predominately of mica-quartz schists and biotite gneisses. The intrusive rocks include quartz porphyry, granite porphyry, and fine-grained monzonitic granites, but only the former two are associated with the tin mineralization. The body of the granite porphyry is concealed but about 30 quartz porphyry dikes crop out at the surface (Fig. 3a, b). From the surface downwards for about 50–100 m, the quartz porphyry dikes progressively converge and finally merge into a single tin-mineralized granite porphyry body (Li 1988). The quartz porphyry consists mainly of quartz phenocrysts (10–20%) and a felsitic matrix (Fig. 4a, b). The concealed granite porphyry is composed of phenocrysts of K-feldspar (15–25%), plagioclase (10–15%), quartz (10–20%), minor biotite (< 2%), and a fine-grained felsic matrix (Fig. 4d, e). Zircon, apatite, monazite, hematite, magnetite, cassiterite, pyrite, sphalerite, and chalcopyrite are common accessory minerals in both the quartz porphyry and the granite porphyry (Fig. 4c, f). The granite porphyry is characterized chemically by high contents of SiO_2 (75.3–75.4 wt%) and $K_2O + Na_2O$ (7.35–8.04 wt%, $K_2O > Na_2O$); low contents of Ca, Mg, and Fe; and A/CNK values of 1.14 to 1.21 (Guan et al. 1988; Zhu et al. 1989).

A total of 65 individual tin orebodies have been defined in the Yinyan deposit (Fu and Chen 1992). These orebodies can be classified into three categories: (1) small-scale vein-style cassiterite–sulfide orebodies that are hosted in the quartz porphyry dikes and in veinlets of the wall rock. These orebodies are distributed at or near the surface and range from 50 to 125 m in length and 1 to 2.5 m in width, with a grade of 0.10–1.83% Sn (Wu 1983). (2) Tin-mineralized granite porphyries, which are the most important Sn orebodies in the Yinyan deposit. These orebodies are located in the middle and upper parts of the concealed granite porphyry body and show a pipe-like shape in profile, and an ellipse-like shape in plan view with an area of 0.06 km^2 (Fig. 3b, c; Guan et al. 1988). Among these orebodies, the largest one is 633–780 m in length, 578–653 m in width, and 11–274 m in thickness, with an average grade of 0.53% Sn. This orebody has about 89% of the tin reserves of the Yinyan deposit (Fu and Chen 1992). Disseminated and stockwork ores are the dominant ore types. (3) Sn–W–Mo orebodies hosted in the middle and lower part of the granite porphyry intrusion (Fig. 3b). These orebodies have most of the W and Mo resources in the Yinyan deposit. The ores are characterized by veinlet dissemination. The major metallic minerals in the ores from the Yinyan deposit are cassiterite, wolframite, molybdenite, bismuthinite, chalcopyrite, pyrite, hematite, wood tin, and small amounts of galena, sphalerite, magnetite, and xenotime. The main gangue minerals are quartz, sericite, muscovite, chlorite, and topaz, followed by fluorite, biotite, and K-feldspar.

The tin-bearing granite porphyry has undergone intense hydrothermal alteration (Zhu et al. 1989). Four zones of alteration can be recognized from bottom to top (Fig. 3b): (1) a weak potassic alteration zone; (2) a protolithionite–quartz greisenization zone; (3) a topaz–quartz greisenization zone, which forms the main mineralized portion; and (4) a phyllic alteration zone (Zhu et al. 1989). These alteration zones are superimposed on each other (Wu 1983). Based on crosscutting relationships and mineral assemblages, we have identified six hydrothermal stages (Fig. 5), as follows.

Stage I (greisenization) This stage is characterized by widespread greisenization of the granite porphyry and is the major tin mineralization stage. The main gangue minerals are muscovite and quartz, along with a small amount of topaz. Quartz phenocrysts can still be observed due to their resistance to alteration (Fig. 6a). Disseminated cassiterite and chalcopyrite are the predominant ore minerals (Fig. 6b), while smaller amounts of magnetite and hematite are also present. The cassiterite occurs mainly as aggregates of anhedral–subhedral grains.

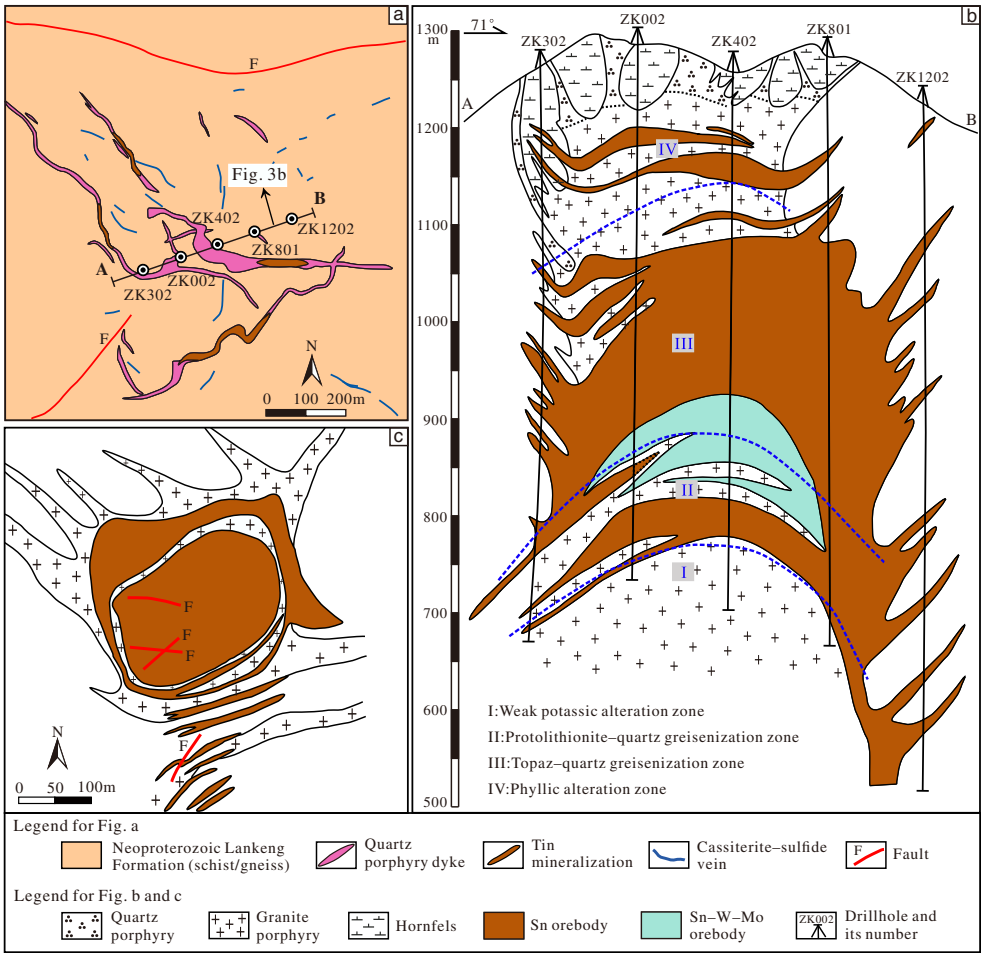

Fig. 3 **a** Schematic geological map of the Yinyan porphyry tin deposit (modified after Li 1988). **b** Cross section along the No. 50 exploration line in the Yinyan tin deposit (adapted from Li 1988 and Zhu et al. 1989). **c** Plan geological view at the 1060 m level in the Yinyan tin deposit (adapted from Guan et al. 1985)

Stage II (cassiterite–topaz–quartz veins) The greisenized granite porphyry (stage I) was cut by the stage II 0.3–2 cm thick cassiterite–topaz–quartz veins/stringers (Fig. 6c). The main minerals in stage II include cassiterite and topaz, followed by quartz, pyrite, and hematite. Cassiterite occurs mainly as aggregates of euhedral grains (Fig. 6d) and the crystals are larger than those of stage I.

Stage III (cassiterite–wolframite–molybdenite veins) The formation of wolframite and molybdenite was initiated in this stage. It is the main stage of W mineralization in the Yinyan deposit. The stage III cassiterite–wolframite–molybdenite veins are cut by stage IV veins of cassiterite and sulfides (Fig. 6e). Wolframite, molybdenite, and cassiterite are the major stage III ore minerals (Fig. 6f), while quartz is the main gangue mineral. The abundant wolframite forms aggregates of euhedral crystals, while cassiterite is disseminated in the veins.

Stage IV (cassiterite–sulfide veins) This stage is characterized by the formation of abundant sulfides and fluorides and is another important stage of tin mineralization in the Yinyan deposit. The major minerals are cassiterite, molybdenite, pyrite, hematite, chalcopyrite, and quartz (Fig. 7a–d), followed by fluorite, topaz, sphalerite, and minor galena and wolframite. Cubes of pyrite, quartz geodes, and purple fluorite are common in the stage IV ores. The cassiterite occurs mainly as aggregates of subhedral–euhedral grains or as disseminated anhedral crystals (Fig. 7b, d).

Stage V (deposition of colloidal minerals) This further important stage of tin mineralization in the Yinyan deposit is characterized by the formation of abundant wood tin (rather than cassiterite) and colloidal hematite. The colloidal hematite and wood tin commonly form botryoidal aggregates or concentric annular crystals, and they enclose minerals that formed earlier, such as wolframite and cassiterite (Fig. 7e, f). The occurrence of wood tin may represent deposition of tin in an environment of low temperature and pressure at the end of mineralization (Lufkin 1977).

Stage VI (quartz–calcite veins) Quartz veins (Fig. 7g) and calcite veins (Fig. 7h) that lack mineralization characterize stage VI, and they represent the last hydrothermal stage in the Yinyan tin deposit.

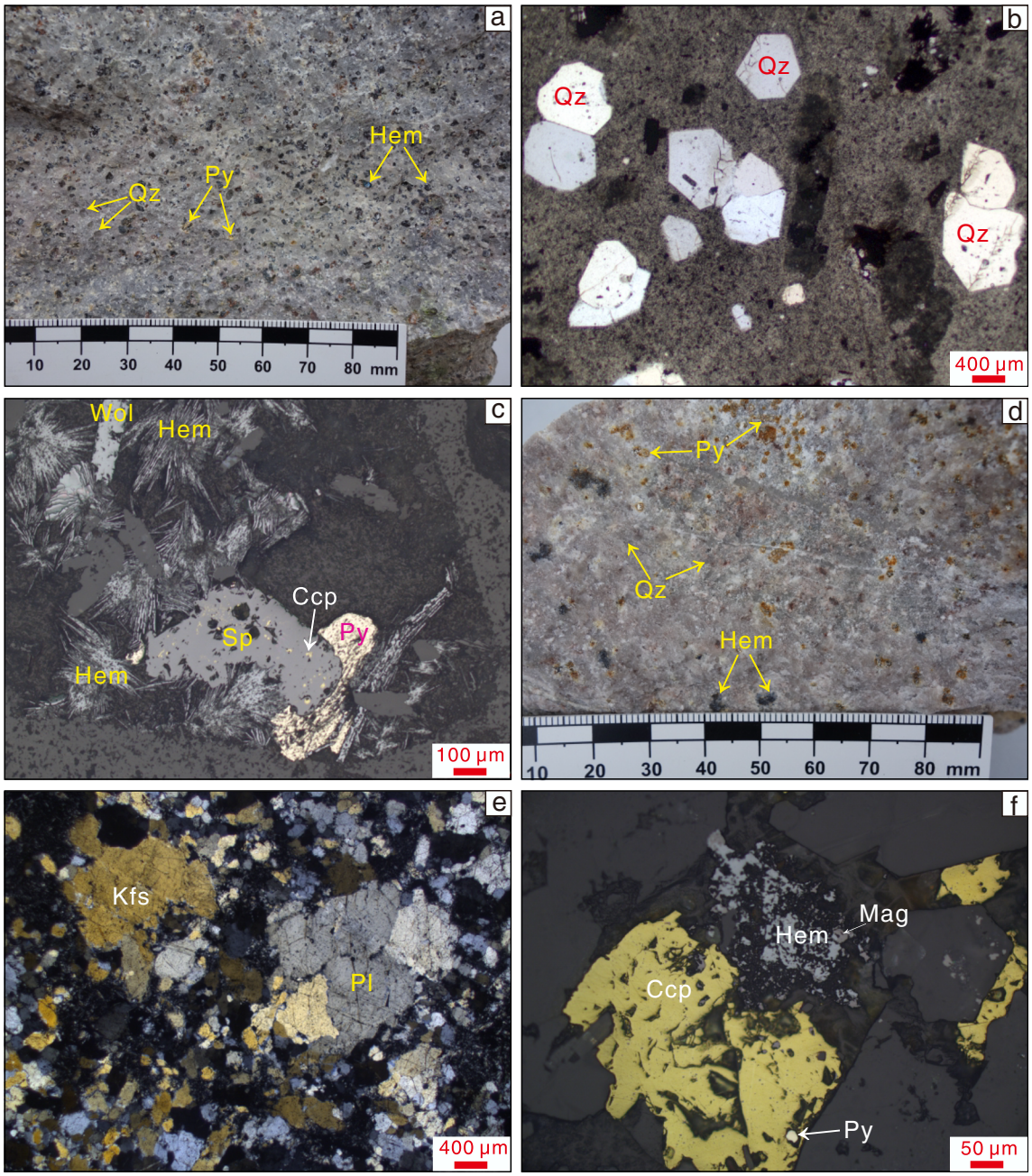

Fig. 4 Photographs and photomicrographs of quartz porphyry (sample Y730, **a**–**c**) and greisenized granite porphyry (sample Y802, **d**–**f**) in the Yinyan tin deposit. **a** Quartz porphyry specimen. **b** Photomicrograph of the quartz porphyry (plane-polarized transmitted light). **c** Representative metallic minerals in the quartz porphyry (reflected light). **d** Granite porphyry specimen. **e** Photomicrograph of the granite porphyry (cross-polarized light). **f** Major metallic minerals in the granite porphyry (reflected light). Mineral abbreviations: Qz = quartz, Kfs = K-feldspar, Pl = plagioclase, Ccp = chalcopyrite, Py = pyrite, Hem = hematite, Mag = magnetite, Wol = wolframite, Sp = sphalerite

Sampling and analytical methods

Whole-rock trace element analysis

One slightly altered quartz porphyry sample and seven specimens of little altered granite porphyry were crushed to 200 mesh and then used for trace element analysis. Fifty milligrams of powdered samples were dissolved in a mixture of HF + HNO_3 in high-pressure Teflon bombs for 48 h at about 190 °C. Trace elements were analyzed on a PerkinElmer Sciex ELAN DRC-e ICP–MS at the State Key Laboratory of Ore Deposit Geochemistry, Institute of Geochemistry, Chinese Academy of Sciences (SKLODG, IGCAS). Rhodium was applied as an internal standard to monitor signal drift. The analytical procedures are described in detail by Qi et al. (2000). The international standards GBPG-1 and OU-6, and

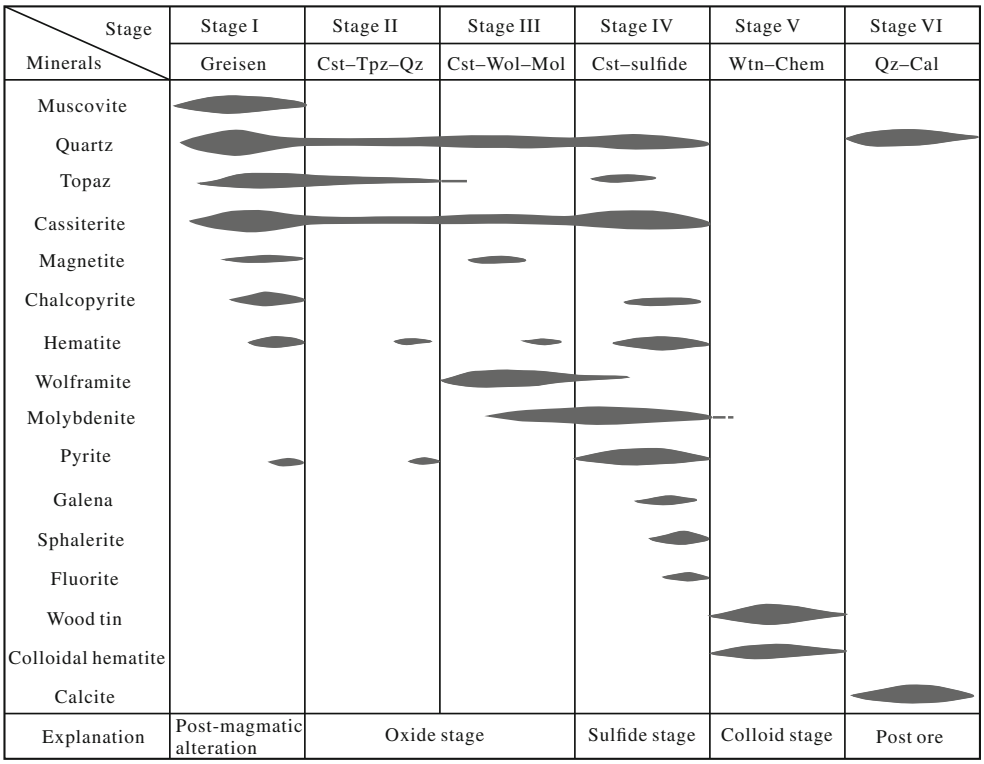

Fig. 5 Simplified paragenetic sequence of mineralization in the Yinyan tin deposit. Abbreviations: Qz = quartz, Cst = cassiterite, Tpz = topaz, Mol = molybdenite, Wol = wolframite, Wtn = wood tin, Chem = colloidal hematite, Cal = calcite

the Chinese national standards GSR-1 and GSR-3, were used for quality control. Analytical precision was typically better than 5%.

LA–ICP–MS zircon U–Pb dating

One slightly altered quartz porphyry sample (Y730; Fig. 4a–c) and one granite porphyry sample with greisenization (Y802; Fig. 4d–f) were collected for zircon separation. After crushing the rock samples, the zircons were separated using conventional heavy liquid and magnetic separation techniques and then handpicked under a binocular microscope. The selected grains were mounted in an epoxy resin disk and polished down to expose the largest crystal areas. Transmitted and reflected light photomicrographs and cathodoluminescence (CL) images were taken to reveal internal structures and allow selection of the best laser ablation spots. CL images of zircon grains were obtained using a JEOL JSM-7800F field emission scanning electron microscopy (SEM) equipped with a MonoCL4 cathodoluminescence detector at the SKLODG, IGCAS.

LA–ICP–MS zircon U–Pb dating was conducted at the SKLODG, IGCAS. Laser sampling was performed using a GeoLas Pro 193 nm ArF excimer laser. An Agilent 7700x ICP–MS instrument was used to acquire ion-signal intensities. Helium was used as carrier gas and was mixed with argon via a T-connector before entering the ICP–MS. Laser ablation conditions were 3 J/cm^2 of laser energy, 5 Hz of ablation frequency, and 24 μm of spot diameter. Zircon 91500 (Wiedenbeck et al. 1995) was used as the external standard for U–Pb dating and analyzed twice every 5–10 analyses. The zircon standard Qinghu was used for quality control and yielded a weighted mean $^{206}Pb/^{238}U$ age of 159.8 ± 1.4 Ma (2σ, $n = 7$), which is in good agreement with the ID-TIMS $^{206}Pb/^{238}U$ age of 159.38 ± 0.12 Ma (2σ) within error (Li et al. 2009). Trace element compositions of zircons were calibrated against multiple reference materials (NIST 610, BHVO-2G, BCR-2G, BIR-1G) combined with Si internal standardization (Liu et al. 2010). Raw data reduction was performed off-line using the ICPMSDataCal program (Liu et al. 2008, 2010). Common Pb correction was not necessary for any of the analyzed zircon grains due to the low signal of common ^{204}Pb and the high $^{206}Pb/^{204}Pb$ ratios. Concordia diagrams and weighted mean age calculations were made using Isoplot 4.15 (Ludwig 2012).

LA–ICP–MS cassiterite U–Pb dating and trace element analysis

Cassiterite from cassiterite–sulfide vein sample Y710 (Fig. 7a, b), cassiterite–sulfide ore sample Y716 (Fig. 7c, d), and cassiterite–topaz–quartz stringer sample Y724 (Fig. 6c, d) were separately selected for LA–ICP–MS U–Pb dating and trace element analysis. The former two samples represent the late hydrothermal stage (stage IV), whereas the last one belongs to the early stage (stage II). The procedures for

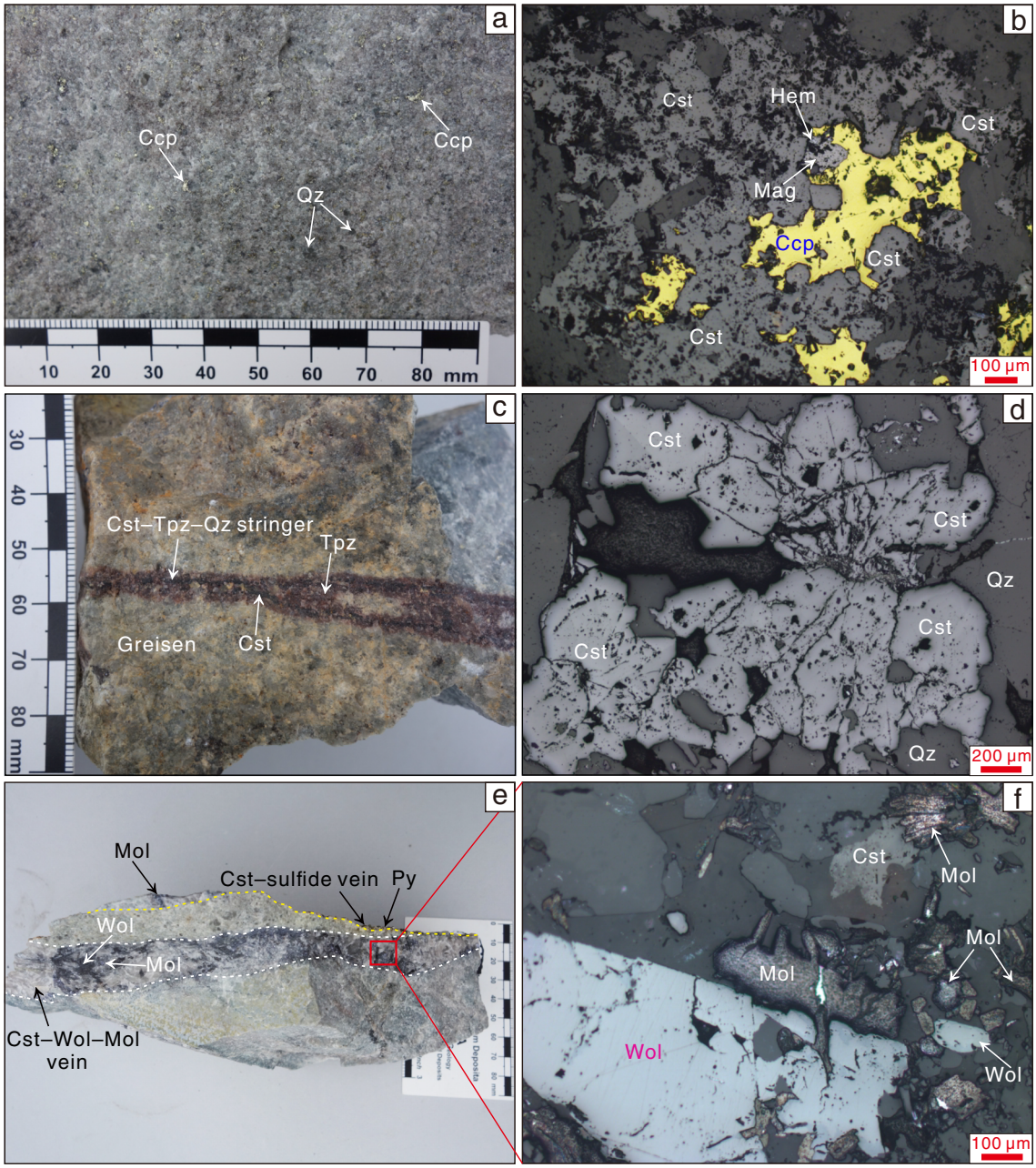

Fig. 6 Representative ores and corresponding photomicrographs (reflected light), and crosscutting relationships of veins in the Yinyan deposit. **a**, **b** Disseminated ore with greisenization. **c**, **d** Greisenization cut by cassiterite–topaz–quartz stringer. **e**, **f** Cassiterite–sulfide vein cutting cassiterite–wolframite–molybdenite vein. Mineral abbreviations: Qz = quartz, Tpz = topaz, Ccp = chalcopyrite, Cst = cassiterite, Hem = hematite, Py = pyrite, Mag = magnetite, Mol = molybdenite, Wol = wolframite

cassiterite separation, grain mounting, and microscopical and CL/BSE photography were similar to those described above for zircon.

LA–ICP–MS cassiterite U–Pb dating and trace element analysis were performed synchronously at the State Key Laboratory for Mineral Deposits Research, Nanjing University, China. The system consisted of an Agilent 7900 ICP–MS coupled with a Resonetics RESOlution S-155 laser. Helium gas carrying the ablated sample aerosol was mixed with argon (carrier gas) and nitrogen (additional di-atomic gas) to enhance sensitivity, and finally flowed into the ICP–MS instrument. Prior to analysis, the system was optimized using reference material NIST SRM610 ablated with a 29 μm spot size and a 5 μm/s scan speed to achieve maximum signal intensity and a low oxidation rate. Cassiterite grains were analyzed using a laser energy density of 4.05 J/cm^2, a spot size of 67 μm, and a repetition rate of 6 Hz. NIST SRM 610 and the in-house cassiterite standard AY-4 were used as external elemental and isotopic calibration standards, respectively. Cassiterite AY-4 has been well analyzed using ID-TIMS and

has a U–Pb age of 158.2 ± 0.4 Ma (Yuan et al. 2011). NIST SRM 610 was analyzed twice for every twelve analyses of cassiterite, and AY-4 was analyzed twice for every six analyses of cassiterite. More details about instrumental parameters and operating conditions are given in Li et al. (2016). Raw data reduction was performed off-line using the ICPMSDataCal 10.1 program (Liu et al. 2010). Tera–Wasserburg concordia diagrams were processed using Isoplot 4.15 (Ludwig 2012). Data uncertainties of isotopic ratios for individual spots are reported at the 1σ level, and the errors of the Tera–Wasserburg lower intercept ages are 2σ (Li et al. 2016).

Molybdenite Re–Os dating

Seven molybdenite-bearing vein samples were selected for separating molybdenite. Molybdenite commonly coexists with cassiterite, wolframite, and/or sulfides. The molybdenite was scraped carefully with a penknife from ore samples and then purified with magnetic separation and floating methods. Thereafter, the molybdenite separates were carefully handpicked under a binocular microscope to reach a purity of > 99% and at last crushed to 200 mesh using an agate mortar.

Molybdenite Re–Os isotopic analyses were carried out in the Re–Os laboratory at the National Research Center of Geoanalysis, Chinese Academy of Geological Sciences, Beijing. Molybdenite separates were digested by HNO_3–HCl in a Carius tube (Shirey and Walker 1995; Smoliar et al. 1996). The tube was then placed in a stainless steel jacket and heated at 230 °C for 10 h. Os was recovered by distilling directly from the sample solution in the Carius tube and was subsequently purified by microdistillation. The Re was separated by solvent extraction and cation exchange resin chromatography. More details of the analytical methods are given by Du et al. (2004). Re and Os concentrations and isotopic compositions were determined using an Element HR–ICP–MS. Average blanks during the analyses were 3.995 pg for Re and 0.09 pg for Os. An average Re–Os age of 222.2 ± 3.4 Ma (95% confidence) was obtained for the molybdenite standard GBW04435 (HLP) used in this study, consistent with the certified value of 221.4 ± 5.6 Ma (Du et al. 2004). The decay constant of ^{187}Re of 1.666×10^{-11} y^{-1} (Smoliar et al. 1996) was used in the age calculations. The Re–Os isochron ages and the weighted average age were calculated using Isoplot 4.15 (Ludwig 2012).

Results

Whole-rock trace elements

The trace element contents of the quartz porphyry and granite porphyry in the Yinyan deposit are summarized in Table 1. The samples have moderate total rare earth element (REE) contents (ΣREE = 153–251 ppm) and show flat chondrite-normalized (Boynton 1984) REE patterns [LREE/HREE = 1.3–2.5, $(La/Yb)_N$ = 0.5–1.2] with strong negative Eu anomalies (Eu/Eu* = 0.003–0.01; Fig. 8a) and the REE tetrad effect. The REE tetrad effect is also supported by the quantification parameter $TE_{1,3}$ (Irber 1999), which is larger than 1.10 and ranges from 1.12 to 1.21 (Table 1). In the primitive mantle-normalized (Sun and McDonough 1989) trace element spider diagram, the rocks show significant negative Ba, P, Sr, Nb, and Ti anomalies and positive U, Th, and Ta anomalies (Fig. 8b). All samples have very low Nb/Ta (1.8–2.4) and Zr/Hf (8.3–10.4) ratios (Table 1).

Zircon U–Pb ages

Zircon grains from the quartz porphyry sample (Y730) are mostly colorless, transparent, and euhedral. They commonly have lengths of 80–160 μm, widths of 20–50 μm, and length/width ratios of 2:1 to 4:1. Most zircon grains exhibit gray to dark luminescence in CL images (Fig. 9a), which may be a result of high U contents. A total of 23 spots on 23 zircon grains were analyzed for sample Y730, and the results are listed in Supplemental Table A. Uncertainty on individual analyses is shown at the 1σ level, and the weighted mean ages are reported at the 2σ level. The analyzed zircon grains have variable U and Th contents in the range of 12,625–34,533 ppm and 1759–5778 ppm, respectively, with Th/U ratios of 0.13 to 0.24. Twenty zircon grains defined a weighted mean $^{206}Pb/^{238}U$ age of 78.5 ± 0.4 Ma (MSWD = 1.7; Fig. 9b), which is perfectly consistent with the concordia U–Pb age of 78.5 ± 0.3 Ma (MSWD = 1.9; Fig. 9a). Two zircon grains yielded older $^{206}Pb/^{238}U$ ages of 89.4 ± 2.2 and 91.6 ± 2.0 Ma perhaps as a result of Pb loss. One inherited zircon grain yielded a $^{206}Pb/^{238}U$ age of 263.8 ± 5.0 Ma.

Zircon grains separated from the greisenized granite porphyry sample (Y802) are smaller than those from the quartz porphyry. Most are anhedral with various shapes, and they display dark to gray luminescence in CL images. As many of these zircon grains were too small to meet the experimental requirements, only ten relatively large euhedral grains with bright luminescence in CL images (Fig. 9c) were analyzed. The analytical results are presented in Supplemental Table A. The U and Th contents of these zircon grains are 247–1067 ppm and 173–1019 ppm, respectively, with Th/U ratios of 0.48 to 0.96. Seven zircon grains yielded a weighted mean $^{206}Pb/^{238}U$ age of 79.2 ± 0.9 Ma (MSWD = 1.1; Fig. 9d), which is in accord with the concordia U–Pb age of 79.3 ± 0.9 Ma (MSWD = 0.94; Fig. 9c). The remaining three zircon grains yielded $^{206}Pb/^{238}U$ ages of 129.3 ± 3.8, 145.6 ± 4.1, and 386 ± 19 Ma, which may imply they were inherited.

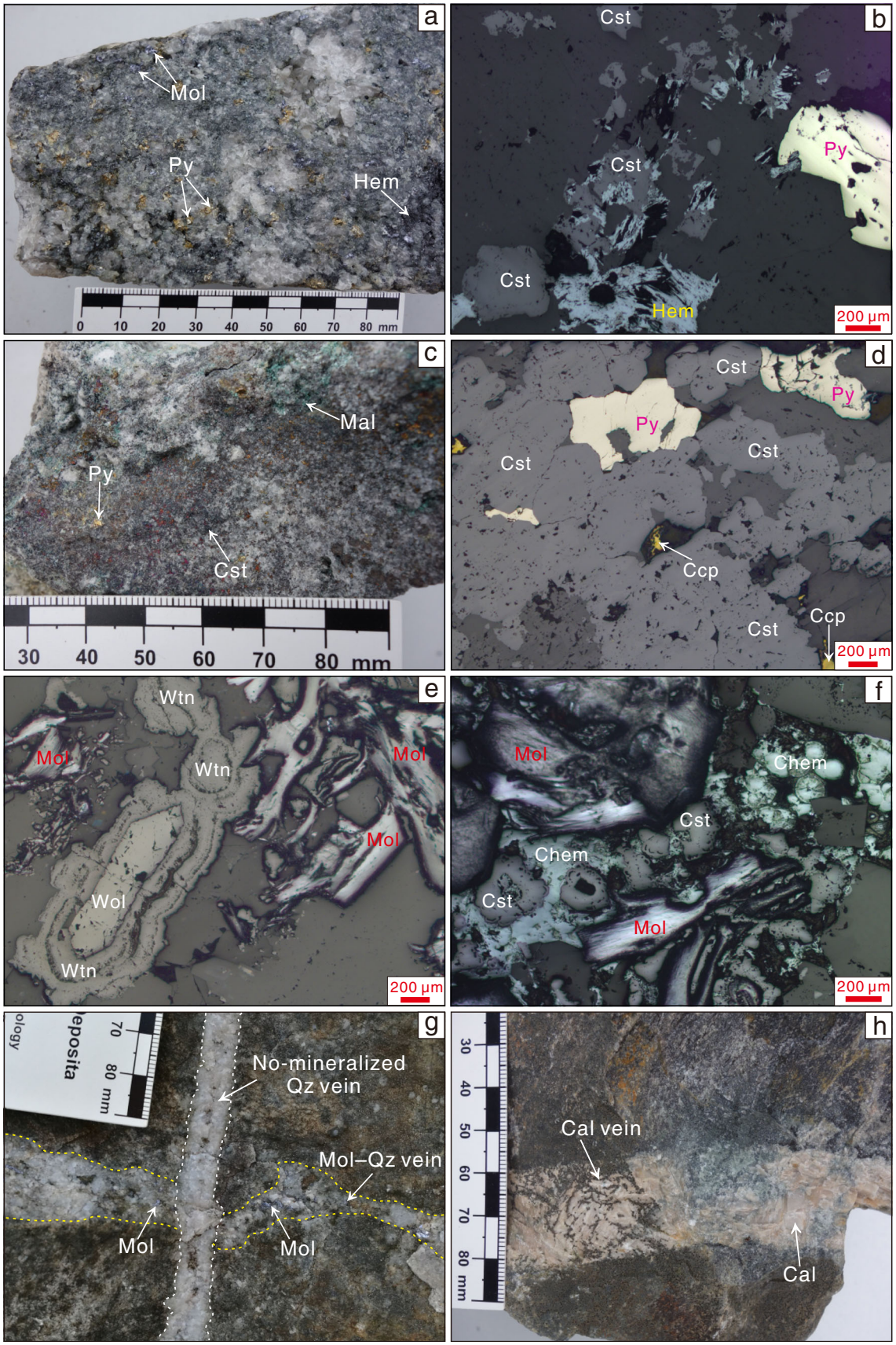
a
Mol
Py
Hem
0 10 20 30 40 50 60 70 80 mm
b
Cst
Cst
Py
Cst
Hem
200 μm
c
Mal
Py
Cst
30 40 50 60 70 80 mm
d
Cst
Py
Py
Cst
Cst
Ccp
Cst
Ccp
200 μm
e
Wtn
Mol
Wtn
Mol
Mol
Wol
Wtn
200 μm
f
Mol
Chem
Cst
Chem
Cst
Mol
200 μm
g
eposita
70 80 mm
No-mineralized
Qz vein
Mol–Qz vein
Mol
Mol
h
30 40 50 60 70 80 mm
Cal vein
Cal

◀◀ **Fig. 7** Photographs and photomicrographs (reflected light) of representative ores in the Yinyan deposit. **a**, **b** Cassiterite–sulfide vein. **c**, **d** Cassiterite–sulfide ore. **e** Wolframite enclosed by wood tin. **f** Cassiterites surrounded by colloidal hematite. **g** Nonmineralized quartz vein cutting molybdenite–quartz vein. **h** Calcite vein. Mineral abbreviations: Cst = cassiterite, Py = pyrite, Mol = molybdenite, Hem = hematite, Wol = wolframite, Ccp = chalcopyrite, Mal = malachite, Wtn = wood tin, Chem = colloidal hematite, Qz = quartz, Cal = calcite

Cassiterite U–Pb ages

The representative CL and BSE images of cassiterite are presented in Fig. 10. It is interesting to note that cassiterite crystals from the three different ore samples are dark in CL image and white in BSE image. No clear-cut zonation can be seen in either CL or BSE images (Fig. 10). A total of 36 spots on 36 cassiterite grains were analyzed for each of the three samples. The analyses were performed on domains where there were no mineral/fluid inclusions or cracks. The LA–ICP–MS U–Pb data are summarized in Supplemental Table B and illustrated in Fig. 11.

Cassiterite from sample Y710 (stage IV cassiterite–sulfide vein) coexists with hematite, wolframite, pyrite, and molybdenite. The cassiterite grains are mostly subhedral to anhedral, 100–500 μm in size, and pale-yellow to dark-brown in color. Eight analyses were discarded because of inclusions or undetectable Pb contents. The remaining 28 spot analyses gave U concentrations of 8.22–406 ppm and Th contents of ≤ 0.02 to 2.12 ppm. These twenty-eight cassiterite grains defined a Tera–Wasserburg U–Pb lower intercept age of 78.5 ± 0.6 Ma (2σ, $n = 28$, MSWD = 1.7; Fig. 11a), which represents the crystallization age of cassiterite in the cassiterite–sulfide vein stage.

The cassiterite from sample Y716 (stage IV cassiterite–sulfide ore) is subhedral to euhedral with bipyramidal crystals that occur as aggregates in the ore. Intergrown minerals include pyrite and chalcopyrite, along with minor wolframite, molybdenite, hematite, galena, and sphalerite. The cassiterite grains are commonly pale-yellow to brown in color and 50–600 μm in size. Six analyses were excluded owing to interference of inclusion signals. The U and Th contents of the other thirty analyzed cassiterite grains ranged from 25.1 to 228.6 ppm and from 0.06 to 1.54 ppm, respectively. The isotopic data for these thirty grains yielded a Tera–Wasserburg U–Pb lower intercept age of 78.6 ± 1.2 Ma (2σ, $n = 30$, MSWD = 2.1; Fig. 11b), which we interpret to be the mineralization age of the cassiterite–sulfide ore.

Cassiterite from sample Y724 (stage II cassiterite–topaz–quartz stringer) are brown to dark-brown in color and 200–800 μm in size. The coarse-grained cassiterite crystals of this sample are generally bipyramidal, while the fine-grained crystals are subhedral to anhedral. A few grains of hematite and chalcopyrite coexist with the cassiterite. Eight analyses were omitted from analysis because of inclusions. The remaining 28 cassiterite grains gave variable U and Th concentrations of 36.9–481 ppm and 0.005–1.43 ppm, respectively. These twenty-eight grains yielded a Tera–Wasserburg U–Pb lower intercept age of 78.2 ± 0.7 Ma (2σ, $n = 28$, MSWD = 3.3; Fig. 11c), which represents the crystallization age of the cassiterite in the cassiterite–topaz–quartz stringer mineralization.

Trace element compositions of cassiterite

The trace element contents of cassiterite from the three different ore samples are listed in Supplemental Table C. Concentrations of each element normally vary over several orders of magnitude. On the whole, the most abundant trace elements in the analyzed cassiterite are Fe (0.22–5.37 wt% FeO), W (22.3–26,885 ppm), and Ti (< 0.01 to 2.15 wt% TiO_2) and to a lesser extent Nb (22.3–12,348 ppm), Ta (4.39–5456 ppm), Zr (15.7–1908 ppm), and Hf (1.00–160 ppm). Mn and Sc have relatively low contents usually lower than 500 and 1000 ppm, respectively. It should be pointed out that most analyzed cassiterite has U concentrations of > 40 to several hundred ppm, which is unusual for cassiterite.

Selected element pairs were plotted on log-scale scatter diagrams (Fig. 12). There is an obvious positive linear correlation between the contents of Zr and Hf (Fig. 12a). The plots of Nb vs. Ta (Fig. 12b), Ti vs. Sc (Fig. 12c), and U vs. (Fe + W) (Fig. 12d) also display positive correlations but with more dispersion. Cassiterite from the early hydrothermal stage (sample Y724, stage II) seems to contain more HFSEs of Zr, Hf, Nb, Ta, and Ti than those from the later hydrothermal stage (samples Y710 and Y716, stage IV) (Fig. 12a–c).

Molybdenite Re–Os ages

The Re–Os concentrations and isotopic compositions of molybdenite separates from seven different types of veined ore are listed in Table 2. The Re and ^{187}Os contents of molybdenite range from 13.4 to 161.6 ppb and from 0.011 to 0.132 ppb, respectively. The seven molybdenite separates yielded model ages that range from 76.7 ± 1.1 to 77.8 ± 1.6 Ma, with a weighted mean age of 77.0 ± 0.5 Ma (MSWD = 0.3). These samples also define a precise ^{187}Re–^{187}Os isochron age of 77.0 ± 0.5 Ma (MSWD = 0.55),

Table 1 Trace element compositions (in ppm) of granites from the Yinyan tin deposit

Sample no.	Y730	Y801	Y802	Y803	Y804	Y805	Y806	Y807
Rock type	Quartz porphyry	Granite porphyry						
Ba	14.8	0.692	0.950	12.1	1.42	21.7	11.0	22.5
Th	28.0	18.4	19.8	15.9	15.3	23.9	20.7	23.9
U	22.1	14.0	18.3	14.6	13.8	16.0	14.2	17.9
Nb	55.2	26.3	24.8	44.6	10.2	44.7	35.4	52.8
Ta	30.0	12.7	11.2	23.2	4.24	21.8	14.8	24.1
Sr	13.1	12.2	9.28	18.9	7.65	8.37	14.9	9.71
P	138	45.1	44.6	45.3	49.0	45.3	46.0	44.9
Nd	23.6	38.4	33.7	22.9	20.6	26.4	24.8	30.6
Zr	63.8	72.5	70.2	57.5	32.6	73.0	51.1	63.8
Hf	7.18	6.95	6.73	6.97	3.21	8.41	5.35	7.07
Sm	8.37	13.8	11.4	8.53	6.75	9.12	8.86	9.72
Eu	0.009	0.024	0.014	0.019	0.015	0.009	0.025	0.029
Ti	63.5	186	123	125	135	125	127	61.7
Y	90.7	154	120	108	65.1	87.9	86.4	72.5
La	21.6	28.8	28.9	17.8	19.8	20.7	18.9	28.9
Ce	59.5	77.6	75.7	48.6	50.0	58.0	54.0	75.6
Pr	7.15	10.1	9.34	6.16	5.90	7.45	6.88	8.95
Nd	23.6	38.4	33.7	22.9	20.6	26.4	24.8	30.6
Sm	8.37	13.8	11.4	8.53	6.75	9.12	8.86	9.72
Eu	0.009	0.024	0.014	0.019	0.015	0.009	0.025	0.029
Gd	8.32	13.9	12.5	9.48	6.39	8.87	8.51	8.70
Tb	1.98	2.88	2.64	2.39	1.51	2.26	2.10	2.02
Dy	16.4	22.1	20.4	20.1	12.6	19.1	17.6	16.3
Ho	3.69	4.79	4.27	4.44	2.74	4.09	3.74	3.38
Er	11.8	14.6	12.7	14.2	8.83	13.0	11.9	10.6
Tm	2.36	2.62	2.31	2.94	1.82	2.62	2.46	2.20
Yb	17.8	18.4	16.2	22.3	14.1	19.8	18.7	16.4
Lu	2.74	2.71	2.41	3.40	2.14	3.00	2.84	2.54
δEu	0.003	0.005	0.004	0.006	0.007	0.003	0.009	0.010
LREE	120	169	159	104	103	122	113	154
HREE	65.1	82.0	73.4	79.3	50.1	72.7	67.9	62.1
Total REE	185	251	232	183	153	194	181	216
LREE/HREE	1.85	2.06	2.17	1.31	2.06	1.67	1.67	2.48
(La/Yb)N	0.82	1.06	1.20	0.54	0.95	0.70	0.68	1.19
Nb/Ta	1.84	2.07	2.21	1.92	2.41	2.05	2.39	2.19
Zr/Hf	8.89	10.43	10.43	8.25	10.16	8.68	9.55	9.02
TE_1	1.25	1.16	1.17	1.18	1.17	1.22	1.22	1.20
TE_3	1.14	1.08	1.11	1.18	1.15	1.20	1.19	1.17
$TE_{1,3}$	1.19	1.12	1.14	1.18	1.16	1.21	1.21	1.18

Note: The subscript N represents chondrite-normalized. $\delta Eu = Eu_N/(Sm_N \times Gd_N)^{1/2}$. $TE_1 = (Ce_N/(La_N^{2/3} \times Nd_N^{1/3}) \times Pr_N/(La_N^{1/3} \times Nd_N^{2/3}))^{1/2}$, $TE_3 = (Tb_N/(Gd_N^{2/3} \times Ho_N^{1/3}) \times Dy_N/(Gd_N^{1/3} \times Ho_N^{2/3}))^{1/2}$, and $TE_{1,3} = (TE_1 \times TE_3)^{1/2}$ (Irber 1999)

which is in excellent agreement with the weighted mean age (Fig. 13). Furthermore, the zero value of the ^{187}Os intercept (initial ^{187}Os) on the ^{187}Re–^{187}Os isochron plot suggests that there was no significant common or initial ^{187}Os in the analyzed molybdenite (Stein et al. 1998, 2001). Our results are also consistent, within error, with the Re–Os isochron age of

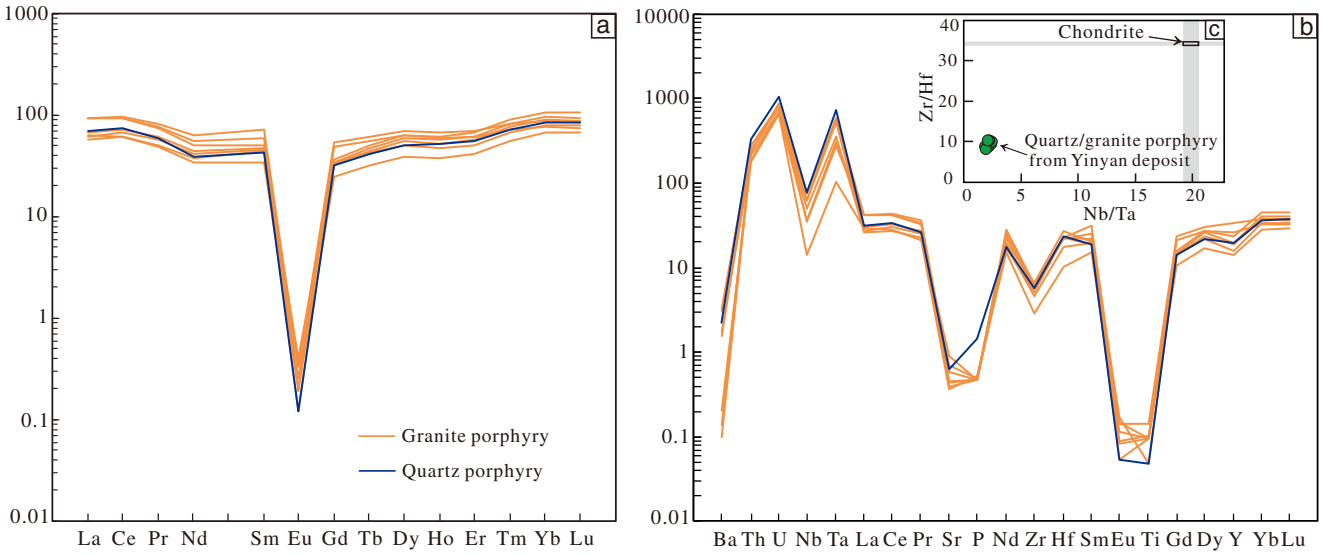

Fig. 8 Chondrite-normalized REE patterns (**a**) and primitive mantle-normalized spider diagrams (**b**) for quartz porphyry and granite porphyry in the Yinyan deposit. The normalization values of chondrite are from Boynton (1984). The primitive mantle-normalized values are from Sun and McDonough (1989). **c** Whole-rock Nb/Ta vs. Zr/Hf diagram for the quartz porphyry and granite porphyry in the Yinyan deposit. The chondritic Zr/Hf and Nb/Ta ratios are from Münker et al. (2003)

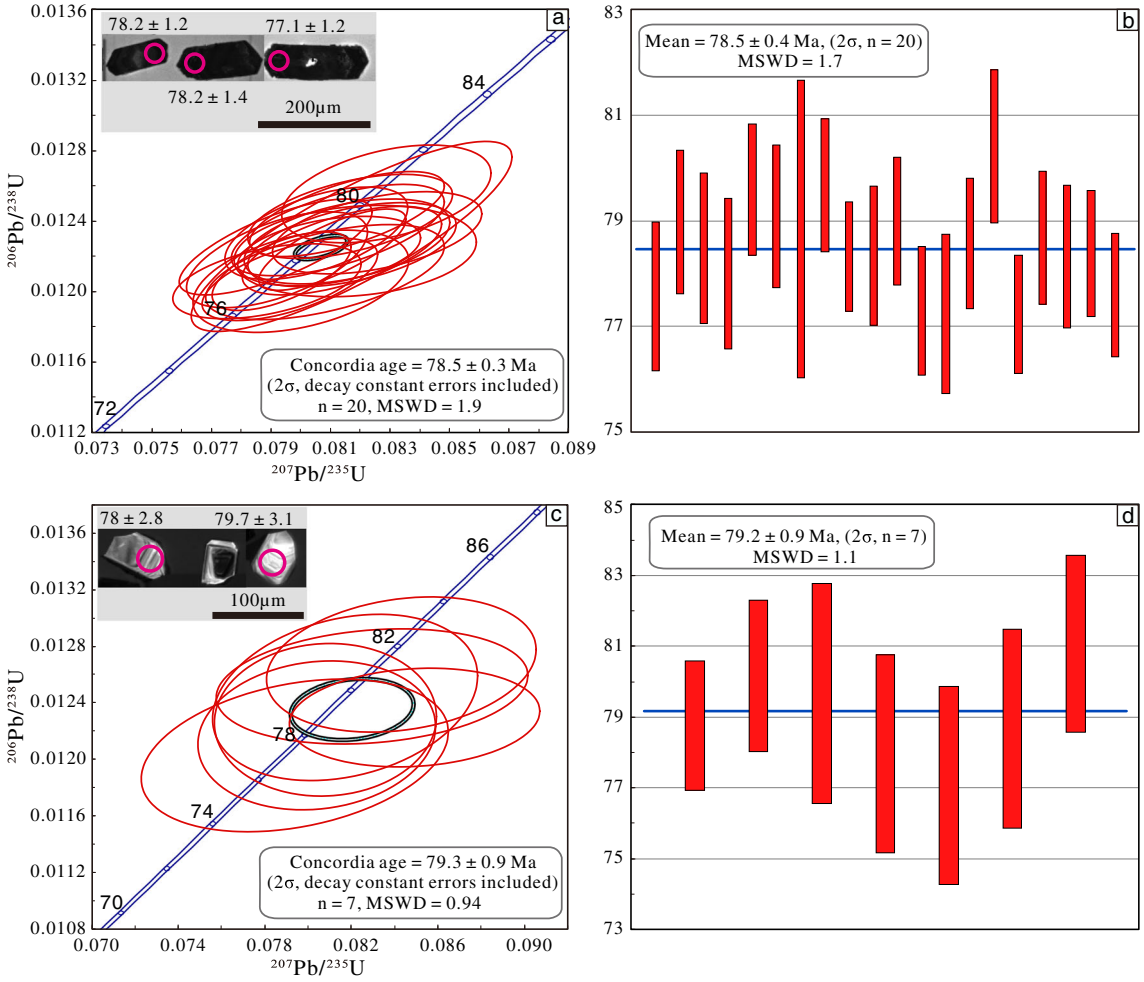

Fig. 9 Zircon U–Pb concordia diagrams and weighted mean ages and cathodoluminescence (CL) images of representative zircon grains from the Yinyan deposit. The circles on the CL images represent laser ablation spots. **a**, **b** Ages of zircon grains from quartz porphyry sample Y730. **c**, **d** Ages of zircon grains from granite porphyry sample Y802

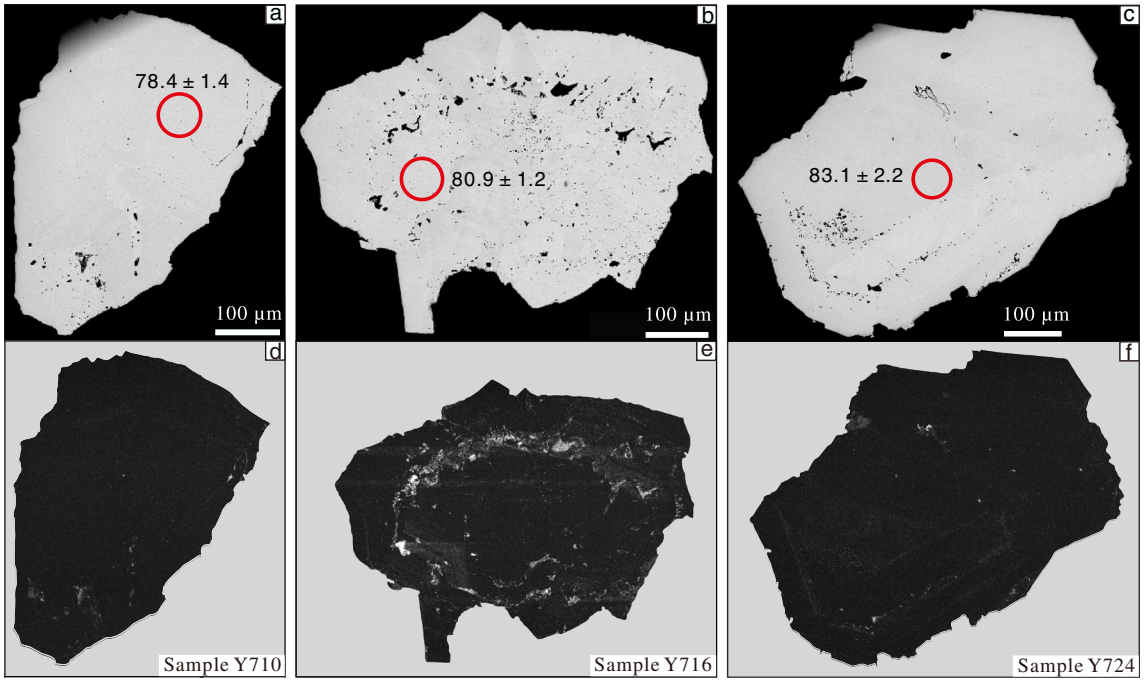

Fig. 10 Backscattered electron (BSE; **a**–**c**) and corresponding cathodoluminescence (CL; **d**–**f**) images of representative cassiterite in the Yinyan deposit from samples Y710 (cassiterite–sulfide vein; **a**, **d**), Y716 (cassiterite–sulfide ore; **b**, **e**), and Y724 (cassiterite–topaz–quartz stringer; **c**, **f**). The cassiterite shows no clear zoning in either the BSE or CL images. Red circles and numbers on the BSE images represent laser ablation spots and the corresponding $^{206}Pb/^{238}U$ ages

78.8 ± 2.6 Ma obtained by Zheng et al. (2016) for the Yinyan tin deposit.

Discussion

Emplacement age of the highly evolved porphyries

Previous geochronological studies on porphyries in the Yinyan deposit are based on whole-rock/single mineral Rb–Sr or K–Ar methods. Guan et al. (1985, 1988) reported whole-rock K–Ar ages of 80, 83, and 92 Ma for three granite porphyry samples and a K–Ar age of 83 Ma for biotite. Hu (1989) provided a whole-rock + feldspar Rb–Sr isochron age of 86.9 ± 6 Ma for the granite porphyry. Shen et al. (1996) obtained an isochron age of 75.6 ± 1.7 Ma for the granite porphyry, also by using the whole-rock Rb–Sr method. As K–Ar and Rb–Sr isotopic systems have relatively low closure temperatures and thus can be easily reset or overprinted by late-stage hydrothermal alteration or tectonothermal events (Stein et al. 2001; Romer et al. 2007), those previous geochronological data span a wide range and may not reveal the true timing of magmatism in the Yinyan deposit. Our new LA–ICP–MS zircon U–Pb dating yielded weighted mean $^{206}Pb/^{238}U$ ages of 78.5 ± 0.4 Ma for the quartz porphyry and 79.3 ± 0.9 Ma for the granite porphyry. These two ages agree well with each other within analytical error. We suggest, therefore, that the quartz porphyry and the granite porphyry in the Yinyan deposit were both emplaced at 78–79 Ma.

The quartz porphyry and the granite porphyry in the Yinyan tin deposit exhibit the typical REE tetrad effect in the chondrite-normalized REE diagram (Fig. 8a), with the quantification parameter ($TE_{1,3}$) of the tetrad effect (Irber 1999) larger than 1.10 (Table 1). It is generally considered that the REE tetrad effect is a characteristic of highly evolved granite (Irber 1999; Jahn et al. 2001; Wu et al. 2007). Moreover, the REE tetrad effect may indicate intense interaction between residual melts and aqueous hydrothermal fluids (probably rich in F and/or Cl) during the late stages of magmatic evolution (Jahn et al. 2001; Zhao et al. 2002; Wu et al. 2004). The presence of abundant fluorite and topaz in the Yinyan ores implies F-rich hydrothermal fluids.

It has been suggested that whole-rock Zr/Hf and Nb/Ta ratios can be used as reliable indicators of the degree of granitic magma differentiation (Bau 1996; Zaraisky et al. 2009; Ballouard et al. 2016; Wu et al. 2017) because both ratios would decrease with increasing magmatic differentiation (Irber 1999; Zaraisky et al. 2009; Chen and Yang 2015; Dostal et al. 2015; Ballouard et al. 2016). The quartz porphyry and the granite porphyry in the Yinyan deposit have whole-rock Zr/Hf (8.89–10.43) and Nb/Ta (1.84–2.07) ratios that are distinctly lower than corresponding chondritic values of 34.3 ± 0.3 and 19.9 ± 0.6 (Münker et al. 2003; Fig. 8c), which indicates advanced magmatic differentiation. Furthermore,

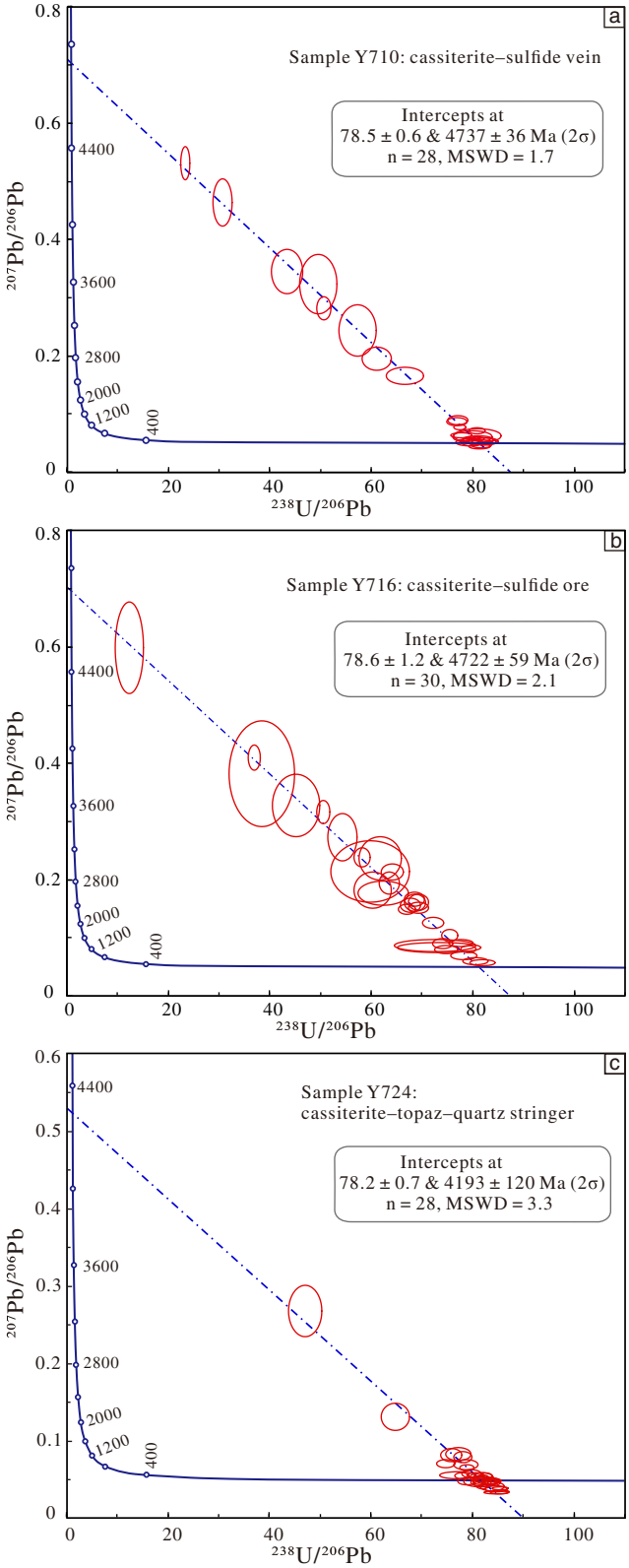

Fig. 11 Tera–Wasserburg concordia diagrams for cassiterite grains from the cassiterite–sulfide vein (**a**), the cassiterite–sulfide ore (**b**), and the cassiterite–topaz–quartz stringer (**c**)

the Nb/Ta ratio of < 5 in peraluminous granites may reveal magmatic–hydrothermal interaction (Ballouard et al. 2016).

Most primary tin deposits are spatially and temporally related to granitic rocks (Taylor 1979; Lehmann 1982, 1987; Hosking 1988). These granitic rocks are often highly evolved (Xu et al. 1984; Heinrich 1990; Lehmann et al. 1990; Wu et al. 2017) and display distinctive geochemical characteristics such as pronounced enrichment in Th, U, Ta, F, and Sn and marked depletion in Ba, Sr, Eu, Ti, Ca, and Zr (Lehmann 1990; Romer and Kroner 2016). As discussed above, these geochemical signatures also characterize the quartz porphyry and the granite porphyry in the Yinyan tin deposit.

Timing of Sn mineralization in the Yinyan deposit

Cassiterite is the major ore mineral in most tin deposits as well as an associated mineral in many tungsten deposits. The closure temperature of the U–Pb isotopic system for cassiterite with a grain size of 1 μm is higher than 500 °C, and for a grain size of 1 mm, it is > 860 °C (Zhang et al. 2011). Due to its refractory nature, cassiterite is highly resistant to post-ore hydrothermal alteration, metamorphism, weathering, acid dissolution, and abrasion (Plimer et al. 1991; Gulson and Jones 1992; Jiang et al. 2004). The homogenization temperatures of fluid inclusions in quartz from different types of ore in the Yinyan deposit range from 260 to 450 °C (Xie et al. 1988). These temperatures are significantly lower than the closure temperature of the cassiterite U–Pb system, which means that the U–Pb isotopic system of the cassiterite in the early veins could not have been disturbed by late-stage hydrothermal fluids. Therefore, our new cassiterite LA–ICP–MS U–Pb ages of 78.5 ± 0.6 Ma (cassiterite–sulfide vein), 78.6 ± 1.2 Ma (cassiterite–sulfide ore), and 78.2 ± 0.7 Ma (cassiterite–topaz–quartz stringer) are reliable. These ages are identical within analytical uncertainties and represent the timing of tin mineralization in Yinyan deposit.

Molybdenite is a common ore mineral in most hydrothermal deposits. It has been proved that the Re–Os chronometer of molybdenite is highly precise and accurate (Stein et al. 1997, 2001; Selby et al. 2002). More importantly, the Re–Os isotope systematics of molybdenite cannot be disturbed by younger hydrothermal, metamorphic, and/or tectonic events, and it is therefore remarkably robust (Stein et al. 1998, 2001; Watanabe and Stein 2000; Selby and Creaser 2001; Bingen and Stein 2003). Therefore, our new ^{187}Re–^{187}Os isochron age of 77.0 ± 0.5 Ma defined by seven molybdenite separates represents the age of the molybdenite mineralization in the Yinyan deposit. Furthermore, the molybdenite Re–Os age is in agreement with the cassiterite U–Pb ages within analytical errors. The consistency of these ages is also in agreement with the fact that molybdenite and cassiterite are paragenetic. Hence, we conclude that the Sn (–Mo–W) mineralization in the Yinyan deposit occurred at 77–78 Ma.

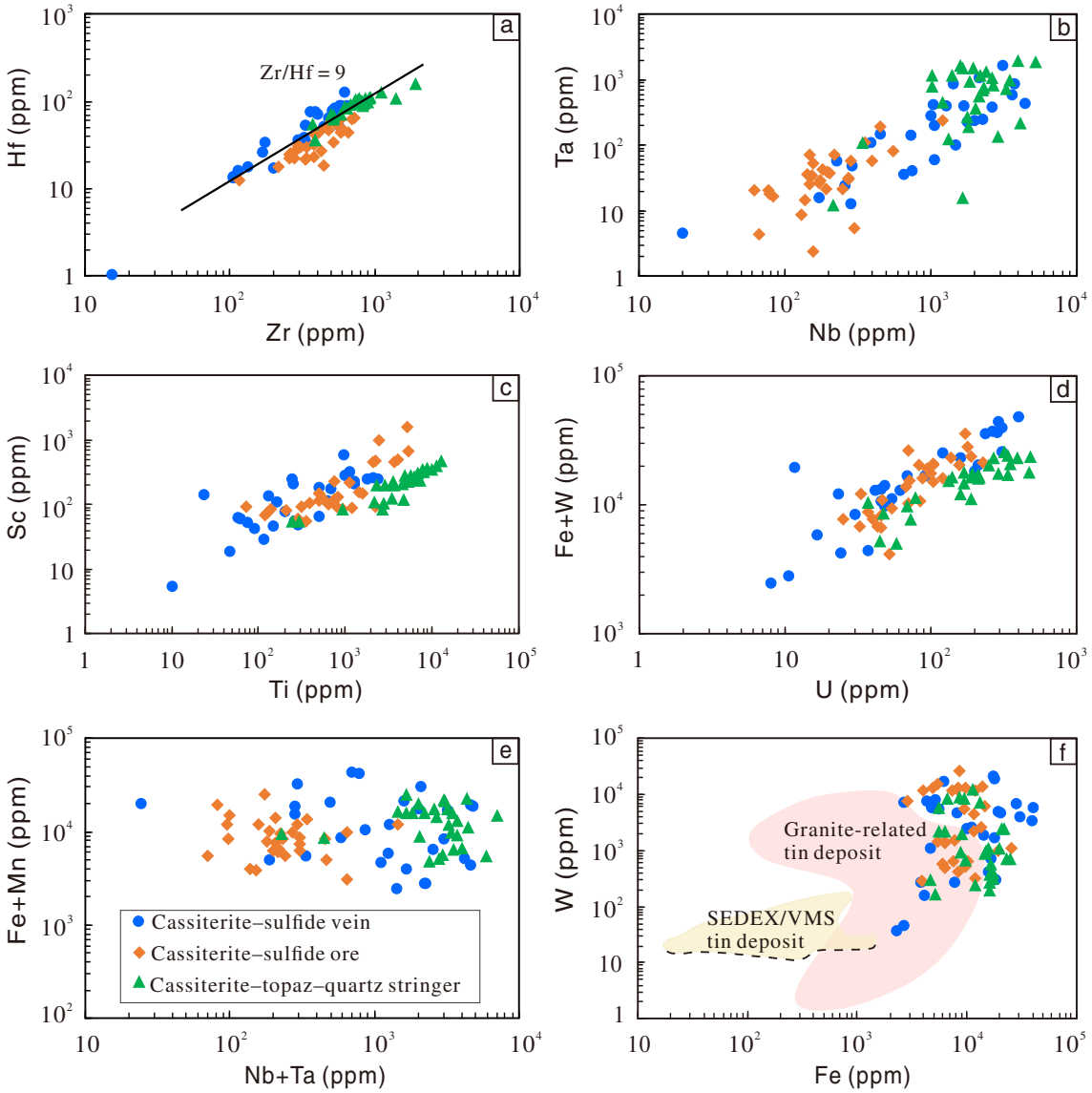

Fig. 12 Log-scale scatter plots of selected trace elements for the cassiterite grains from three different ore samples in the Yinyan deposit. On the W vs. Fe bivariate diagram, the colored domains of granite-related and SEDEX/VMS-type tin deposits are from Guo et al. (2018a)

Our new cassiterite U–Pb and molybdenite Re–Os ages for the mineralization agree well with the zircon U–Pb ages for the magmatism within analytical errors. These data convincingly indicate that the tin mineralization in the Yinyan deposit is

Table 2 Re–Os isotope compositions for molybdenite from the Yinyan tin deposit

Sample	Weight (g)	Re (ng/g)		Os (ng/g)		^{187}Re (ng/g)		^{187}Os (ng/g)		Model age (Ma)	
		Measured	2σ	Measured	2σ	Measured	2σ	Measured	2σ	Measured	2σ
Y701	0.20247	145.1	1.7	0.0006	0.0004	91.19	1.10	0.1171	0.0009	77.06	1.33
Y719	0.20114	146.2	1.8	0.0001	0.0000	91.88	1.16	0.1184	0.0007	77.31	1.32
Y720	0.20075	161.6	2.4	0.0013	0.0000	101.6	1.5	0.1318	0.0013	77.82	1.58
Y721	0.20056	150.9	1.6	0.0002	0.0000	94.85	1.01	0.1218	0.0007	77.06	1.21
Y723	0.20039	87.33	0.72	0.0003	0.0000	54.89	0.45	0.0701	0.0005	76.65	1.10
Y727	0.20039	13.40	0.19	0.0001	0.0000	8.42	0.12	0.0108	0.0001	77.10	1.65
Y728	0.20133	114.9	1.1	0.0001	0.0001	72.22	0.67	0.0925	0.0005	76.83	1.13

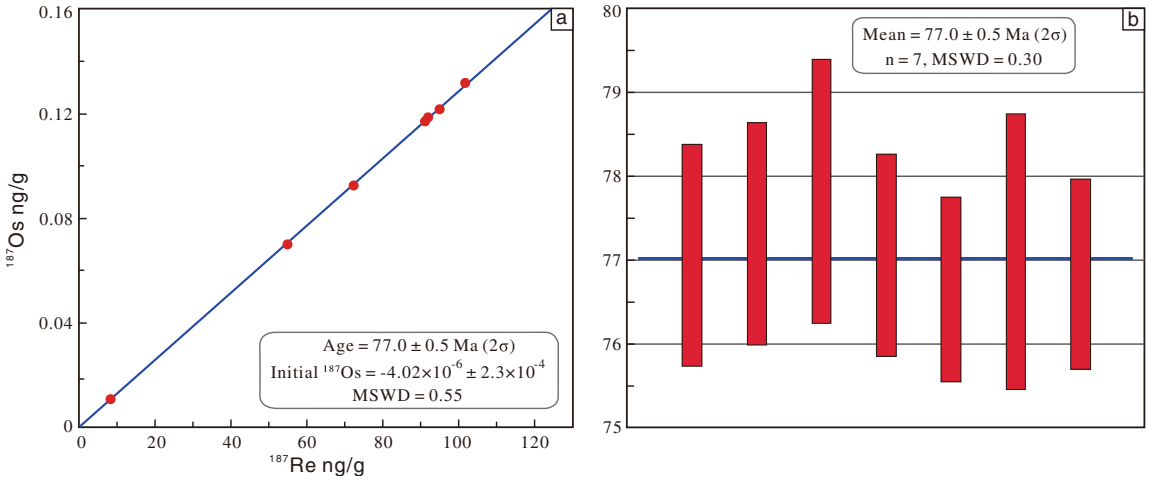

Fig. 13 Re–Os isochron and weighted average model age diagrams for molybdenite separates from seven different ore samples in the Yinyan deposit

genetically related to the granitic magmatism, and the magmatism and mineralization both occurred nearly simultaneously at ca. 77–79 Ma (Fig. 14).

Trace element geochemistry of cassiterite

Due to their similar charges, radii, and ion coordination to Sn^{4+}, significant amounts of Ti and other trace elements such as W, Fe, Mn, Nb, Ta, Zr, Hf, and In, among others, can be incorporated in cassiterite (Cohen et al. 1985; Möller et al. 1988; Neiva 1996; Lerouge et al. 2017). The plots of Fe + Mn vs. Nb + Ta (Fig. 12e) and W vs. Fe (Fig. 12f) show no significant correlations. Therefore, the commonly proposed substitution mechanisms of $W^{6+} + 2Fe^{3+} = 3Sn^{4+}$, $(Fe, Mn)^{2+} + 2(Nb, Ta)^{5+} = 3(Sn, Ti)^{4+}$, and $Fe^{3+} + (Nb, Ta)^{5+} = 2(Sn, Ti)^{4+}$ (Černý and Ercit 1985; Černý et al. 1985; Cohen et al. 1985; Möller et al. 1988) cannot be confirmed in the cassiterite of the Yinyan deposit. The differences in the Nb, Ta, Zr, and Hf contents of the early (stage II) and late stage (stage IV) cassiterite may have resulted from the decrease in temperature, which is supported by the previous study that fluid inclusions in quartz from cassiterite–sulfide stage (stage IV) have the lowest homogenization temperature of 260–320 °C (Xie et al. 1988).

The trace element composition of cassiterite may reveal the mineralization type and the environment of ore formation (Steveson and Taylor 1973; Plimer et al. 1991; Murciego et al. 1997; Hennigh and Hutchinson 1999). Fe and W are both effective in distinguishing granite-affiliated cassiterite from the cassiterite of SEDEX/VMS deposits (Taylor 1979; Hennigh and Hutchinson 1999; Guo et al. 2018a). Cassiterite from the Yinyan tin deposit has very high concentrations of W and Fe and falls within the field of granite-related tin deposits (Fig. 12f) on the W vs. Fe bivariate discrimination plot (Guo et al. 2018a). The Zr/Hf ratio of cassiterite can be used to discriminate different types of mineralization (Möller and Dulski 1983). Cassiterite from pegmatites is characterized by Zr/Hf ratios of ~ 5, whereas cassiterite in hydrothermal mineralization has Zr/Hf ratios of ~ 30 (Möller and Dulski 1983). The cassiterite from albite–spodumene pegmatites in the Western Kunlun Orogen has Zr/Hf ratios of ~ 6, with a maximum value of 7.3 (Feng et al. 2019), whereas the Zr/Hf ratios of cassiterite from the world-class Gejiu tin district vary from 12.5 for greisen-hosted cassiterite to 16.7 for granite-disseminated cassiterite (Cheng et al. 2019). The Zr and Hf contents of cassiterite from the Yinyan tin deposit display a clear positive linear correlation (Fig. 12a), with Zr/Hf ratios approximating 9.

It is interesting to note that the cassiterite in the Yinyan tin deposit has very high U concentrations (Supplemental Table B) and shows dark luminescence in CL images (Fig. 10). Most of the cassiterite grains have U concentrations that are > 40 ppm, with maximum U content of 481 ppm and average U content of 141 ppm. To the best of our knowledge, the U concentrations in cassiterite from other representative Sn (±W) deposits around the world rarely exceed 40 ppm (Zagruzina et al. 1987; Yuan et al. 2008, 2011; Zhang et al. 2017c, d; Guo et al. 2018a, b; Neymark et al. 2018; Cheng et al. 2019). The high U concentrations in the Yinyan cassiterite may reveal high U contents in the ore-forming fluids, which in turn would indicate that the precursor magma was highly evolved because U is a strongly incompatible element. CL zoning patterns under the SEM can reveal trace element distributions in cassiterite (Hall and Ribbe 1971; Wille et al. 2018; Cheng et al. 2019). The intensity of the luminescence is governed by the interplay between the luminescence activators (Ti and W) and quenchers (such as Fe) (Hall and Ribbe 1971; Farmer et al. 1991), e.g., the presence of Fe with W suppresses the W-activated emission, while Fe occurring with Ti enhances the probability of luminescence transitions (Hall and Ribbe 1971; Farmer et al. 1991). Furthermore, quenching combinations of (Si and Fe) or (Nb and Ta) in cassiterite may

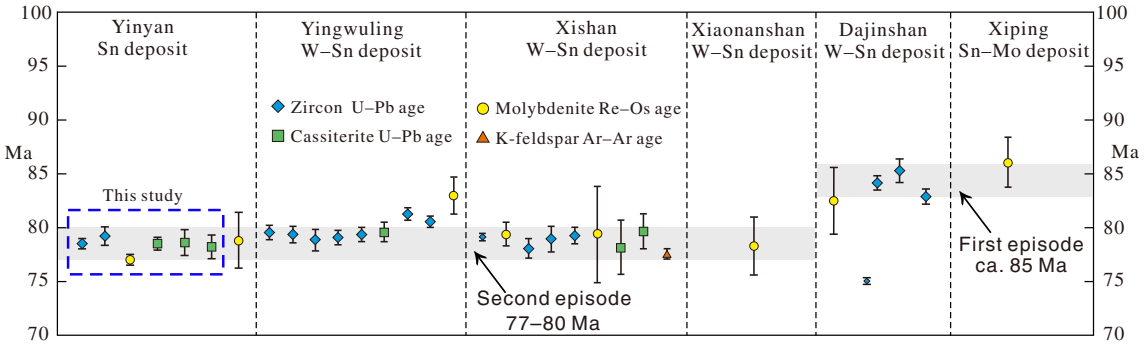

Fig. 14 Age spectra of Late Cretaceous granitic magmatism and the associated W–Sn mineralization in western Guangdong Province. The data sources of Sn–W deposits age are shown in Supplemental Table D

have a negative effect on the CL intensity (Hall and Ribbe 1971; Wille et al. 2018). Guo et al. (2018a) concluded that the Ti content of cassiterite is the key controller of luminescence intensity, whereas the activator W provides weak luminescence in SEM–CL images. However, Wille et al. (2018) suggested the luminescence of cassiterite is quenched when Fe is present with Ti. In the case of the cassiterite of the Yinyan deposit, its high Fe, Nb, and Ta contents may be the key factors that underlie the dark luminescence in CL images (Fig. 10), but this needs to be confirmed by more comprehensive studies.

Two Sn–W metallogenic events and the possible tectonic setting in western Guangdong

There are many Sn (±W) deposits adjacent to the Yinyan tin deposit, e.g., the Yinwuling, Xiaonanshan, Dajinshan, and Xishan W–Sn deposits, and the Xiping Sn–Mo polymetallic deposit (Figs. 1b and 2). Combining the zircon and cassiterite U–Pb, and molybdenite Re–Os geochronological data of these deposits published in recent years (Supplemental Table D), it is evident that there are two Sn–W metallogenic events in this region, one at ca. 85 Ma and the other at 77–80 Ma (Fig. 14).

As early as the 1980s, it had been realized that the peak of isotopic ages at 80–95 Ma in the Late Cretaceous represented the most important period of tin mineralization in South China (Xu and Zhu 1988). The world-class Gejiu and Dulong (southeastern Yunnan) and Dachang (northwestern Guangxi) tin-polymetallic deposits, together with the foregoing Sn–W deposits in western Guangdong, all formed in this period. In the past few years, and on the basis of numerous precise geochronological data, Cheng et al. (2016) concluded that 80–100 Ma, with a peak at 83–90 Ma, was the most important period of large-scale Sn–W mineralization and associated magmatic activity in the regions of southeast Yunnan and northeast Vietnam. Zhang et al. (2017b, 2018, 2019) went on to define an E–W-trending 80–100 Ma belt of Sn–W mineralization that extended from western Guangdong westwards to southeastern Yunnan in South China. For comparative purposes, we compiled the zircon U–Pb ages of granitic rocks and the molybdenite Re–Os, mica Ar–Ar, and cassiterite U–Pb ages of the associated Sn–W deposits in southeast Yunnan, Guangxi, and western Guangdong (Supplemental Table D). The data set clearly shows that all these Sn–W deposits and the related magmatism formed in a period of 75–100 Ma (Fig. 1b).

Deciphering the tectonic setting of ore deposit formation is likely to cause controversy. This issue is a particularly knotty one in the case of Yinyan and neighboring Sn–W deposits because they formed in the Late Cretaceous at a location that was at the junction of the Pacific and Tethyan tectonic domains (Zhou et al. 2008; Wang et al. 2011; Xu et al. 2018). As mentioned above, the Yinyan Sn deposit and adjacent Sn–W deposits in western Guangdong are part of an extensive 75–100 Ma Sn–W mineralization belt, and one would expect, therefore, that all these Sn–W deposits shared the same or similar geodynamic settings. Nevertheless, the tectonic setting of these deposits has remained a subject of hot debate. The predominant view has been that the formation of these Sn–W deposits was related to the subduction of the paleo-Pacific Plate (Zhou and Li 2000; Zhou et al. 2006; Mao et al. 2013; Zheng et al. 2015, 2016, 2017a, b; Cheng et al. 2016), but more recently, it has been proposed that either Neo-Tethyan subduction was responsible for the formation of these deposits (Sun 2016; Zhang et al. 2017b, 2018, 2019; Sun et al. 2018; Xu et al. 2018), or that Neo-Tethyan subduction was the main controlling factor with some contribution from the Pacific system (Wang et al. 2011). Here, we lean toward the Neo-Tethyan model for the following reasons. Firstly, the 75–100 Ma Sn–W mineralization belt is almost perpendicular to the direction of the paleo-Pacific Plate subduction (Zhou and Li 2000; Zhou et al. 2006; Sun et al. 2007; Mao et al. 2011, 2013; Liu et al. 2017), whereas this belt is parallel to the northern subducting boundary of the Neo-Tethyan Plate during Cretaceous (Sun 2016; Liu et al. 2017; Zhang et al. 2017a; Sun et al. 2018). This is similar to the situation in South America where the important Bolivian tin belt and the famous porphyry Cu–Au belt are both parallel to the subducting

boundary of the offshore plate (Mlynarczyk and Williams-Jones 2005; Romer and Kroner 2016). Secondly, it has been suggested that the E–W-trending Hainan marginal arc belonged to the Tethyan tectonic realm in the Cretaceous (Fang 2016). The magmatism and subduction-related orogeny in the Hainan marginal arc reached a peak at the transition from the Early to the Late Cretaceous, and the arc-related magmatic–sedimentary activities continued until ~70 Ma (Fang 2016). The western Guangdong Province is geographically close to the Hainan marginal arc in the Late Cretaceous, and thus, the 75–100 Ma Sn–W deposits were more likely controlled by the Tethyan tectonic system. Finally, the 75–100 Ma Sn–W mineralization belt is temporally (western part also spatially) close to the ca. 62–76 Ma tin mineralization that was controlled by the Tethyan tectonic domain in the Tengchong–Baoshan region in western Yunnan (Xu et al. 2018), which makes it even more likely that the 75–100 Ma Sn–W deposits in South China were also related to the Tethyan tectonic system.

Conclusions

(1) The quartz porphyry and granite porphyry associated with tin mineralization in the Yinyan deposit are highly evolved and emplaced at ca. 78–79 Ma. The tin mineralization in the Yinyan deposit occurred at ca. 77–78 Ma, and it has close temporal and spatial relationships with the porphyry magmatism.

(2) The most abundant trace elements in cassiterite from the Yinyan deposit are Fe, W, Ti, and U, with lesser amounts of Nb, Ta, Zr, and Hf. The high Fe, Nb, and Ta contents of the cassiterite may be responsible for its dark luminescence in CL images.

(3) During the Late Cretaceous, there were two Sn–W metallogenic events in western Guangdong. One occurred at ca. 85 Ma and the other at 77–80 Ma. These two episodes are part of a large-scale 75–100 Ma Sn–W mineralization event that geographically extended from southeastern Yunnan through Guangxi to western Guangdong. Neo-Tethyan subduction, rather than subduction of the paleo-Pacific Plate, was responsible for this large-scale Sn–W mineralization event in South China.

Acknowledgments We are grateful to Saihu Lu from the 933 team of the Geology Bureau for Nonferrous Metals of Guangdong Province for his support during the field geological investigation. We also appreciate the help given by Jing Hu and Yan Huang during the whole-rock trace element analyses, Yanwen Tang for his guidance in LA–ICP–MS zircon U–Pb dating, and Huan Hu for her assistance during the LA–ICP–MS cassiterite U–Pb dating. This paper has benefited from constructive suggestions and comments from the editor and two anonymous reviewers.

Funding information This work was financially supported by the National Key Research and Development Program of China (Grant No. 2016YFC0600405) and the National Natural Science Foundation of China (Grant Nos. 41572074 and 41273049).

References

Ballouard C, Poujol M, Boulvais P, Branquet Y, Tartèse R, Vigneresse JL (2016) Nb–Ta fractionation in peraluminous granites: a marker of the magmatic–hydrothermal transition. Geology 44:231–234

Bau M (1996) Controls on the fractionation of isovalent trace elements in magmatic and aqueous systems: evidence from Y/Ho, Zr/Hf, and lanthanide tetrad effect. Contrib Mineral Petrol 123:323–333

Bingen B, Stein H (2003) Molybdenite Re–Os dating of biotite dehydration melting in the Rogaland high-temperature granulites, S Norway. Earth Planet Sci Lett 208:181–195

Boynton WV (1984) Cosmochemistry of the rare earth elements: meteorite studies. In: Henderson P (ed) Rare earth element geochemistry. Elsevier, Amsterdam, pp 63–114

Černý P, Ercit TS (1985) Some recent advances in the mineralogy and geochemistry of Nb and Ta in rare-element granitic pegmatites. Bull Mineral 108:499–532

Černý P, Roberts WL, Ercit TS, Chapman R (1985) Wodginite and associated oxide minerals from the Peerless pegmatite, Pennington County, South Dakota. Am Mineral 70:1044–1049

Charvet J, Shu LS, Shi YS, Guo LZ, Faure M (1996) The building of South China: collision of Yangzi and Cathaysia blocks, problems and tentative answers. J SE Asian Earth Sci 13:223–235

Chen JY, Yang JH (2015) Petrogenesis of the Fogang highly fractionated I-type granitoids: constraints from Nb, Ta, Zr and Hf. Acta Petrol Sin 31:846–854 **(in Chinese with English abstract)**

Chen ZH, Sheng JF, Liu LJ, Wang DH, Liang T, Wang CH (2015) A preliminary review of metallogenic regularity of tin deposits in China. Acta Geol Sin (Engl Edn) 89:1021–1035

Chen CH, Liu YH, Lee CY, Sano Y, Zhou HW, Xiang H, Takahata N (2017) The Triassic reworking of the Yunkai massif (South China): EMP monazite and U-Pb zircon geochronologic evidence. Tectonophysics 694:1–22

Cheng YB, Mao JW, Liu P (2016) Geodynamic setting of Late Cretaceous Sn–W mineralization in southeastern Yunnan and northeastern Vietnam. Solid Earth Sci 1:79–88

Cheng YB, Spandler C, Kemp A, Mao JW, Rusk B, Hu Y, Blake K (2019) Controls on cassiterite (SnO_2) crystallization: evidence from cathodoluminescence, trace-element chemistry, and geochronology at the Gejiu Tin District. Am Mineral 104:118–129

Cohen AJ, Adekeye JID, Hapke B, Partlow DP (1985) Interstitial Sn^{2+} in synthetic and natural cassiterite crystals. Phys Chem Miner 12:363–369

Dostal J, Kontak DJ, Gerel O, Shellnutt JG, Fayek M (2015) Cretaceous ongonites (topaz-bearing albite-rich microleucogranites) from Ongon Khairkhan, Central Mongolia: products of extreme magmatic fractionation and pervasive metasomatic fluid: rock interaction. Lithos 236–237:173–189

Du AD, Wu SQ, Sun DZ, Wang SX, Qu WJ, Markey R, Stain H, Morgan J, Malinovskiy D (2004) Preparation and certification of Re–Os dating reference materials: molybdenites HLP and JDC. Geostand Geoanal Res 28:41–52

Fang NQ (2016) A new model on the Mesozoic "South China Sea" (SCS): reconstructing the Hainan marginal arc and recognizing the Tethyan SCS. Earth Sci Front 23:107–119 **(in Chinese with English abstract)**

Farmer CB, Searl A, Halls C (1991) Cathodoluminescence and growth of cassiterite in the composite lodes at South Crofty Mine, Cornwall, England. Mineral Mag 55:447–458

Feng YG, Liang T, Yang XQ, Zhang Z, Wang YQ (2019) Chemical evolution of Nb–Ta oxides and cassiterite in phosphorus-rich albite–spodumene pegmatites in the Kangxiwa–Dahongliutan pegmatite field, Western Kunlun Orogen, China. Minerals 9:166

Fu CL, Chen WK (1992) The descriptive model for the Yinyan porphyry tin deposit, Xinyi, Guangdong Province. Geol China 1:20–23 **(in Chinese)**

Guan XF, Zhou YQ, Xiao JH, Liang SH, Li JM (1985) Yinyan porphyry tin deposit—a new type of tin deposits in China. Acta Geol Sin 59: 155–162 **(in Chinese with English abstract)**

Guan XF, Shou YQ, Xiao JH, Liang SZ, Li JM (1988) A new type of tin deposit—the Yinyan porphyry tin deposit in China. In: Hutchison CS (ed) Geology of tin deposits in Asia and the Pacific. Springer, New York, pp 487–494

Gulson BL, Jones MT (1992) Cassiterite: potential for direct dating of mineral deposits and a precise age for the Bushveld Complex granites. Geology 20:355–358

Guo J, Zhang RQ, Li CY, Sun WD, Hu YB, Kang DM, Wu JD (2018a) Genesis of the Gaosong Sn–Cu deposit, Gejiu district, SW China: constraints from in situ LA–ICP–MS cassiterite U–Pb dating and trace element fingerprinting. Ore Geol Rev 92:627–642

Guo J, Zhang RQ, Sun WD, Ling MX, Hu YB, Wu K, Luo M, Zhang LC (2018b) Genesis of tin-dominant polymetallic deposits in the Dachang district, South China: insights from cassiterite U–Pb ages and trace element compositions. Ore Geol Rev 95:863–879

Hall MR, Ribbe PH (1971) An electron microprobe study of luminescence centers in cassiterite. Am Mineral 56:31–45

Han KY, Xu KJ, Gao LZ, Ding XZ, Ren LD, Liu YX, Pang JF (2017) U–Pb age and Lu–Hf isotope of detrital zircons from the metasedimentary rocks in the Yunkai region and their geological significance. Acta Petrol Sin 33:2939–2956 **(in Chinese with English abstract)**

Heinrich CA (1990) The chemistry of hydrothermal tin (-tungsten) ore deposition. Econ Geol 85:457–481

Hennigh Q, Hutchinson RW (1999) Cassiterite at Kidd Creek: an example of volcanogenic massive sulfide-hosted tin mineralization. Econ Geol Monogr 10:431–440

Hosking KFG (1988) The world's major types of tin deposit. In: Hutchison CS (ed) Geology of tin deposits in Asia and the Pacific. Springer, New York, pp 3–49

Hu XZ (1989) The origin and petrology of the Yinyan tin-bearing granite porphyry. Geochimica 3:251–259 **(in Chinese with English abstract)**

Hua RM, Mao JW (1999) A preliminary discussion on the Mesozoic metallogenic explosion in east China. Mineral Deposits 18:300–308 **(in Chinese with English abstract)**

Huang XD, Zhang DY (1989) Geochemical zoning pattern of the Yinyan tin deposit. J Geochem Explor 33:109–119

Irber W (1999) The lanthanide tetrad effect and its correlation with K/Rb, Eu/Eu*, Sr/Eu, Y/Ho, and Zr/Hf of evolving peraluminous granite suites. Geochim Cosmochim Acta 63:489–508

Jahn BM, Wu FY, Capdevila R, Martineau F, Zhao ZH, Wang YX (2001) Highly evolved juvenile granites with tetrad REE patterns: the Woduhe and Baerzhe granites from the Great Xing'an Mountains in NE China. Lithos 59:171–198

Jiang SY, Yu JM, Lu JJ (2004) Trace and rare-earth element geochemistry in tourmaline and cassiterite from the Yunlong tin deposit, Yunnan, China: implication for migmatitic–hydrothermal fluid evolution and ore genesis. Chem Geol 209:193–213

Ke XZ, Zhou D, Long WG, Wang J, Xu DM, Tian Y, Jin W (2018) Indosinian metamorphism and anatexis in Yunkai Massif: evidences from zircon geochronology and Hf isotopes of migmatites and gneisses. Earth Sci 43:2249–2275 **(in Chinese with English abstract)**

Kong ZG, Liang T, Mao JW, Xu SF, Xu HB, Yan PP, Jin XY (2018) Study on perogenesis of granodiorite, metallogenic epoch and petrogenetic-metallogenetic setting in the Zhuxiling tungsten polymetallic deposit, southern Anhui Province, China. Acta Petrol Sin 34:2632–2656 **(in Chinese with English abstract)**

Lehmann B (1982) Metallogeny of tin: magmatic differentiation versus geochemical heritage. Econ Geol 77:50–59

Lehmann B (1987) Tin granites, geochemical heritage, magmatic differentiation. Geol Rundsch 76:177–185

Lehmann B (1990) Metallogeny of tin. Lecture notes in earth sciences 32. Springer, Berlin, pp 1–211

Lehmann B, Ishihara S, Michel H, Miller J, Rapela C, Sanchez A, Tistl M, Winkelmann L (1990) The Bolivian tin province and regional tin distribution in the Central Andes: a reassessment. Econ Geol 85: 1044–1058

Lerouge C, Gloaguen E, Wille G, Bailly L (2017) Distribution of In and other rare metals in cassiterite and associated minerals in Sn ± W ore deposits of the western Variscan Belt. Eur J Mineral 29:739–753

Li ZQ (1988) A discussion on geological features and genesis of porphyry tin ore deposit in Yinyan Guangdong Province. Earth Sci (J China Univ Geosci) 13:603–612 **(in Chinese with English abstract)**

Li XH, Liu Y, Li QL, Guo CH, Chamberlain KR (2009) Precise determination of Phanerozoic zircon Pb/Pb age by multicollector SIMS without external standardization. Geochem Geophys Geosyst 10: Q04010

Li CY, Zhang RQ, Ding X, Ling MX, Fan WM, Sun WD (2016) Dating cassiterite using laser ablation ICP–MS. Ore Geol Rev 72:313–322

Liu YS, Hu ZC, Gao S, Günther D, Xu J, Gao CG, Chen HH (2008) In situ analysis of major and trace elements of anhydrous minerals by LA–ICP–MS without applying an internal standard. Chem Geol 257:34–43

Liu YS, Gao S, Hu ZC, Gao CG, Zong KQ, Wang DB (2010) Continental and oceanic crust recycling-induced melt–peridotite interactions in the Trans-North China Orogen: U–Pb dating, Hf isotopes and trace elements in zircons from mantle xenoliths. J Petrol 51:537–571

Liu SF, Gurnis M, Ma PF, Zhang B (2017) Reconstruction of northeast Asian deformation integrated with western Pacific plate subduction since 200 Ma. Earth-Sci Rev 175:114–142

Liu P, Mao JW, Santosh M, Xu LG, Zhang RQ, Jia LH (2018) The Xiling Sn deposit, eastern Guangdong Province, Southeast China: a new genetic model from $^{40}Ar/^{39}Ar$ muscovite and U–Pb cassiterite and zircon geochronology. Econ Geol 113:511–530

Ludwig KR (2012) User's manual for Isoplot 3.75: a geochronological toolkit for Microsoft Excel. Berkeley Geochronology Center Special Publication No. 5, pp 1–75

Lufkin JL (1977) Chemistry and mineralogy of wood-tin, Black Range, New Mexico. Am Mineral 62:100–106

Mao JW, Xie GQ, Guo CL, Yuan SD, Cheng YB, Chen YC (2008) Spatial-temporal distribution of Mesozoic ore deposits in South China and their metallogenic settings. Geol J China Univ 14:510–526 **(in Chinese with English abstract)**

Mao JW, Chen MH, Yuan SD, Guo CL (2011) Geological characteristics of the Qinhang (or Shihang) metallogenic belt in South China and spatial-temporal distribution regularity of mineral deposits. Acta Geol Sin 85:636–658 **(in Chinese with English abstract)**

Mao JW, Cheng YB, Chen MH, Pirajno F (2013) Major types and time–space distribution of Mesozoic ore deposits in South China and their geodynamic settings. Miner Deposita 48:267–294

Mao JW, Xiong BK, Liu J, Pirajno F, Cheng YB, Ye HS, Song SW, Dai P (2017) Molybdenite Re/Os dating, zircon U–Pb age and geochemistry of granitoids in the Yangchuling porphyry W–Mo deposit (Jiangnan tungsten ore belt), China: implications for petrogenesis, mineralization and geodynamic setting. Lithos 286–287:35–52

Mlynarczyk MSJ, Williams-Jones AE (2005) The role of collisional tectonics in the metallogeny of the Central Andean tin belt. Earth Planet Sci Lett 240:656–667

Möller P, Dulski P (1983) Fractionation of Zr and Hf in cassiterite. Chem Geol 40:1–12

Möller P, Dulski P, Szacki W, Malow G, Riedel E (1988) Substitution of tin in cassiterite by tantalum, niobium, tungsten, iron and manganese. Geochim Cosmochim Acta 52:1497–1503

Münker C, Pfänder JA, Weyer S, Büchl A, Kleine T, Mezger K (2003) Evolution of planetary cores and the Earth-Moon system from Nb/Ta systematics. Science 301:84–87

Murciego A, Sanchez AG, Dusausoy Y, Pozas JMM, Ruck R (1997) Geochemistry and EPR of cassiterites from the Iberian Hercynian Massif. Mineral Mag 61:357–365

Neiva AMR (1996) Geochemistry of cassiterite and its inclusions and exsolution products from tin and tungsten deposits in Portugal. Can Mineral 34:745–768

Neymark LA, Holm-Denoma CS, Moscati RJ (2018) In situ LA–ICPMS U–Pb dating of cassiterite without a known-age matrix-matched reference material: examples from worldwide tin deposits spanning the Proterozoic to the Tertiary. Chem Geol 483:410–425

Pan GT, Xiao QH, Lu SN, Den JF, Feng YM, Zhang KX, Zhang ZY, Wang FG, Xing GF, Hao GJ, Feng YF (2009) Subdivision of tectonic units in China. Geol China 36:1–28 **(in Chinese with English abstract)**

Peng SM, Fu LF, Zhou GQ (1995a) Tectonic evolution of Yunkai Massif and its shearing anatectic origin of gneissic granitic rocks. China Univ Geosci Press, Wuhan, pp 1–167 **(in Chinese with English abstract)**

Peng SM, Peng SB, Shao JG (1995b) Geological features and tectonic evolution of peripheral faults around Yunkai Massif. Guangdong Geol 10:9–16 **(in Chinese with English abstract)**

Plimer IR, Lu J, Kleeman JD (1991) Trace and rare earth elements in cassiterite — sources of components for the tin deposits of the Mole Granite, Australia. Mineral Deposita 26:267–274

Qi L, Hu J, Gregoire DC (2000) Determination of trace elements in granites by inductively coupled plasma mass spectrometry. Talanta 51:507–513

Romer RL, Kroner U (2016) Phanerozoic tin and tungsten mineralization–tectonic controls on the distribution of enriched protoliths and heat sources for crustal melting. Gondwana Res 31: 60–95

Romer RL, Thomas R, Stein HJ, Rhede D (2007) Dating multiply overprinted Sn-mineralized granites—examples from the Erzgebirge, Germany. Miner Deposita 42:337–359

Selby D, Creaser RA (2001) Re–Os geochronology and systematics in molybdenite from the Endako porphyry molybdenum deposit, British Columbia, Canada. Econ Geol 96:197–204

Selby D, Creaser RA, Hart CJR, Rombach CS, Thompson JFH, Smith MT, Bakke AA, Goldfarb RJ (2002) Absolute timing of sulfide and gold mineralization: a comparison of Re–Os molybdenite and Ar–Ar mica methods from the Tintina Gold Belt, Alaska. Geology 30: 791–794

Shao JG, Peng SM, Peng SB (1995) $^{40}Ar/^{36}Ar$–$^{39}Ar/^{36}Ar$ isochron dating for peripheral faults of Yunkai massif. Guangdong Geol 10:34–40 **(in Chinese with English abstract)**

Shen WZ, Wang DZ, Liu CS (1996) Isotope geochemical characteristics and material sources of tin-bearing porphyries in South China. Acta Geol Sin (Engl Edn) 9:181–192

Shirey SB, Walker RJ (1995) Carius tube digestion for low-blank rhenium–osmium analysis. Anal Chem 67:2136–2141

Smoliar MI, Walker RJ, Morgan JW (1996) Re–Os ages of group IIA, IIIA, IVA, and IVB iron meteorites. Science 271:1099–1102

Stein HJ, Markey RJ, Morgan JW, Du A, Sun Y (1997) Highly precise and accurate Re–Os ages for molybdenite from the East Qinling molybdenum belt, Shaanxi Province, China. Econ Geol 92:827–835

Stein HJ, Sundblad K, Markey RJ, Morgan JW, Motuza G (1998) Re–Os ages for Archean molybdenite and pyrite, Kuittila-Kivisuo, Finland and Proterozoic molybdenite, Kabeliai, Lithuania: testing the chronometer in a metamorphic and metasomatic setting. Miner Deposita 33:329–345

Stein HJ, Markey RJ, Morgan JW, Hannah JL, Scherstén A (2001) The remarkable Re–Os chronometer in molybdenite: how and why it works. Terra Nova 13:479–486

Steveson BG, Taylor RG (1973) Trace element content of some cassiterites from Eastern Australia. Proc R Soc Queensland 84:43–54

Sun WD (2016) Initiation and evolution of the South China Sea: an overview. Acta Geochim 35:215–225

Sun SS, McDonough WF (1989) Chemical and isotopic systematics of oceanic basalts: implications for mantle composition and processes. In: Saunders AD, Norry MJ (eds) Magmatism in the ocean basins. Geol Soc London Spec Pub 42, pp 313–345

Sun WD, Ding X, Hu YH, Li XH (2007) The golden transformation of the Cretaceous plate subduction in the West Pacific. Earth Planet Sci Lett 262:533–542

Sun WD, Yang XY, Fan WM, Wu FY (2012) Mesozoic large scale magmatism and mineralization in South China: preface. Lithos 150:1–5

Sun WD, Lin CT, Zhang LP, Liao RQ, Li CY (2018) The formation of the South China Sea resulted from the closure of the Neo-Tethys: a perspective from regional geology. Acta Petrol Sin 34:3467–3478

Taylor RG (1979) Geology of tin deposits. Elsevier, Amsterdam, pp 1–543

Wan YS, Liu DY, Wilde SA, Cao JJ, Chen B, Dong CY, Song B, Du LL (2010) Evolution of the Yunkai Terrane, South China: evidence from SHRIMP zircon U–Pb dating, geochemistry and Nd isotope. J Asian Earth Sci 37:140–153

Wang ZW, Zhou YZ, Zhang HH, Zhou HW (1998) The basement evolution and mineralization of Yunkai Massif, South China. Prog Precambrian Res 21:45–53 **(in Chinese with English abstract)**

Wang YJ, Fan WM, Zhao GC, Ji SC, Peng TP (2007) Zircon U–Pb geochronology of gneissic rocks in the Yunkai massif and its implications on the Caledonian event in the South China Block. Gondwana Res 12:404–416

Wang DS, Liu JL, Tran MD, Ngyuen QL, Guo Q, Wu WB, Zhang ZC, Zhao ZD (2011) Geochronology, geochemistry and tectonic significance of granites in the Tĩnh Túc W–Sn ore deposits, Northeast Vietnam. Acta Petrol Sin 27:2795–2808 **(in Chinese with English abstract)**

Wang CY, Han RS, Huang JG, Xu SH, Ren T (2019) The ^{40}Ar–^{39}Ar dating of biotite in ore veins and zircon U–Pb dating of porphyrtic granite dyke in the Nanyangtian tungsten deposit in SE Yunnan, China. Ore Geol Rev 114:103133

Watanabe Y, Stein HJ (2000) Re–Os ages for the Erdenet and Tsagaan Suvarga porphyry Cu–Mo deposits, Mongolia, and tectonic implications. Econ Geol 95:1537–1542

Wiedenbeck M, Allé P, Corfu F, Griffin WL, Meier M, Oberli F, Vonquadt A, Roddick JC, Speigel W (1995) Three natural zircon

standards for U–Th–Pb, Lu–Hf, trace element and REE analyses. Geostand Newslett 19:1–23

Wille G, Lerouge C, Schmidt U (2018) A multimodal microcharacterisation of trace-element zonation and crystallographic orientation in natural cassiterite by combining cathodoluminescence, EBSD, EPMA and contribution of confocal Raman-in-SEM imaging. J Microsc 270:309–317

Wu ZL (1983) Geological features of the Yinyan porphyry tin deposit. Geol Explor 7:21–25 **(in Chinese)**

Wu FY, Sun DY, Jahn BM, Wilde S (2004) A Jurassic garnet-bearing granitic pluton from NE China showing tetrad REE patterns. J Asian Earth Sci 23:731–744

Wu FY, Li XH, Yang JH, Zheng YF (2007) Discussions on the petrogenesis of granites. Acta Petrol Sin 23:1217–1238 **(in Chinese with English abstract)**

Wu FY, Liu XC, Ji WQ, Wang JM, Yang L (2017) Highly fractionated granites: recognition and research. Sci China Earth Sci 60:1201–1219

Xie YH, Zhao R, Li RM, Wang YL (1988) Physical-chemical conditions and material sources for mineralization of the Yinyan porphyry tin deposit. Mineral Deposits 7:42–49 **(in Chinese with English abstract)**

Xu KQ, Zhu JC (1988) Time–space distribution of tin/tungsten deposits in South China and controlling factors of mineralization. In: Hutchison CS (ed) Geology of tin deposits in Asia and the Pacific. Springer, New York, pp 265–277

Xu KQ, Sun N, Wang DZ, Hu SX, Liu YJ, Ji SY (1984) Petrogenesis of the granitoids and their metallogenetic relations in South China. In: Xu KQ, Tu GC (eds) Geology of granites and their metallogenetic relations. Science Press, Beijing, pp 1–32

Xu R, Deng J, Cheng HY, Cui XL, Wang CB (2018) Geochronology, geochemistry and geodynamic setting of Late Cretaceous magmatism and Sn mineralization in the western South China and Tengchong–Baoshan. Acta Petrol Sin 34:1271–1284 **(in Chinese with English abstract)**

Yan QH, Li SS, Qiu ZW, Wang H, Wei XP, Pei L, Dong R, Zhang XY (2017) Geochronology, geochemistry and Sr–Nd–Hf–S–Pb isotopes of the Early Cretaceous Taoxihu Sn deposit and related granitoids, SE China. Ore Geol Rev 89:350–368

Yu JS, Gui XT, Li PZ, Yuan C (1998) Isotope and trace element geochemistry of granitoid plutons in Yangchun basin, Guangdong. Guangdong Geol 13:1–10 **(in Chinese with English abstract)**

Yuan SD, Peng JT, Hu RZ, Li HM, Shen NP, Zhang DL (2008) A precise U–Pb age on cassiterite from the Xianghualing tin-polymetallic deposit (Hunan, South China). Miner Deposita 43:375–382

Yuan SD, Peng JT, Hao S, Li HM, Geng JZ, Zhang DL (2011) In situ LA–MC–ICP–MS and ID–TIMS U–Pb geochronology of cassiterite in the giant Furong tin deposit, Hunan Province, South China: new constraints on the timing of tin-polymetallic mineralization. Ore Geol Rev 43:235–242

Zagruzina IA, Pinskii EM, Savinova IB (1987) Uranium in cassiterite of tin deposits. Int Geol Rev 29:94–109

Zaraisky GP, Aksyuk AM, Devyatova VN, Udoratina OV, Chevychelov VY (2009) The Zr/Hf ratio as a fractionation indicator of rare-metal granites. Petrology 17:25–45

Zhang DL, Peng JT, Hu RZ, Yuan SD, Zheng DS (2011) The closure of U–Pb isotope system in cassiterite and its reliability for dating. Geol Rev 57:549–554 **(in Chinese with English abstract)**

Zhang LP, Hu YB, Liang JL, Ireland T, Chen YL, Zhang RQ, Sun SJ, Sun WD (2017a) Adakitic rocks associated with the Shilu copper–molybdenum deposit in the Yangchun Basin, South China, and their tectonic implications. Acta Geochim 36:132–150

Zhang LP, Zhang RQ, Hu YB, Liang JL, Ouyang ZX, He JJ, Chen YX, Guo J, Sun WD (2017b) The formation of the Late Cretaceous Xishan Sn–W deposit, South China: geochronological and geochemical perspectives. Lithos 290–291:253–268

Zhang RQ, Lehmann B, Seltmann R, Sun WD, Li CY (2017c) Cassiterite U–Pb geochronology constrains magmatic–hydrothermal evolution in complex evolved granite systems: the classic Erzgebirge tin province (Saxony and Bohemia). Geology 45:1095–1098

Zhang RQ, Lu JJ, Lehmann B, Li CY, Li GL, Zhang LP, Guo J, Sun WD (2017d) Combined zircon and cassiterite U–Pb dating of the Piaotang granite-related tungsten–tin deposit, southern Jiangxi tungsten district, China. Ore Geol Rev 82:268–284

Zhang LP, Zhang RQ, Wu K, Chen YX, Li CY, Hu YB, He JJ, Liang JL, Sun WD (2018) Late Cretaceous granitic magmatism and mineralization in the Yingwuling W–Sn deposit, South China: constraints from zircon and cassiterite U–Pb geochronology and whole–rock geochemistry. Ore Geol Rev 96:115–129

Zhang LP, Zhang RQ, Chen YX, Sun SJ, Liang JL, Sun WD (2019) Geochronology and geochemistry of the Late Cretaceous Xinpeng granitic intrusion, South China: implication for Sn–W mineralization. Ore Geol Rev 113:103075

Zhao YM, Wu LS (2007) Tungsten and tin mineral resources map of China (1:5,000,000). Geol Publ House, Beijing **(in Chinese)**

Zhao ZH, Xiong XL, Han XD, Wang YX, Wang Q, Bao ZW, Jahn B (2002) Controls on the REE tetrad effect in granites: evidence from the Qianlishan and Baerzhe granites, China. Geochem J 36:527–543

Zheng W, Mao JW, Zhao HJ, Zhao CS, Lin WP, Ouyang ZX, Wu XD, Tian Y (2015) A preliminary study of minerogenetic series and geodynamic background of polymetallic deposits in Yangchun Basin of western Guangdong Province. Mineral Deposits 34:465–487 **(in Chinese with English abstract)**

Zheng W, Mao JW, Zhao CS, Ouyang HG, Wang XY (2016) Re–Os geochronology of molybdenite from Yinyan porphyry Sn deposit in South China. Resour Geol 66:63–70

Zheng W, Mao JW, Zhao HJ, Ouyang HG, Zhao CS, Yu XF (2017a) Geochemistry, Sr–Nd–Pb–Hf isotopes systematics and geochronological constrains on petrogenesis of the Xishan A-type granite and associated W–Sn mineralization in Guangdong Province, South China. Ore Geol Rev 88:739–752

Zheng W, Mao JW, Zhao HJ, Zhao CS, Yu XF (2017b) Two Late Cretaceous A-type granites related to the Yingwuling W–Sn polymetallic mineralization in Guangdong province, South China: implications for petrogenesis, geodynamic setting, and mineralization. Lithos 274–275:106–122

Zhong ZQ, You ZD, Zhou HW, Han YJ (1996) The evolution and basic structural framework of the basement of the Yunkai uplift. Reg Geol China 1:36–43 **(in Chinese with English abstract)**

Zhou XM, Li WX (2000) Origin of Late Mesozoic igneous rocks in southeastern China: implications for lithosphere subduction and underplating of mafic magmas. Tectonophysics 326:269–287

Zhou GQ, Zheng YM, Wu AS (1996) Pre-Sinian strata in the Yunkai area in Guangdong and Guangxi Province. Reg Geol China 4:296–303 **(in Chinese with English abstract)**

Zhou XM, Sun T, Shen WZ, Shu LS, Niu YL (2006) Petrogenesis of Mesozoic granitoids and volcanic rocks in South China: a response to tectonic evolution. Episodes 29:26–33

Zhou D, Sun Z, Chen HZ, Xu HH, Wang WY, Pang X, Cai DS, Hu DK (2008) Mesozoic paleogeography and tectonic evolution of South China Sea and adjacent areas in the context of Tethyan and Paleo-Pacific interconnections. Island Arc 17:186–207

Zhou XY, Yu JH, Wang LJ, Shen LW, Zhang CH (2015) Compositions and formation of the basement metamorphic rocks in Yunkai

terrane, western Guangdong Province, South China. Acta Petrol Sin 31:855–882 **(in Chinese with English abstract)**

Zhu ZS, Zhu JC, Xu KQ (1989) Geology, geochemistry and genesis of Yinyan porphyry tin deposit. Chin J Geochem 8:374–384